

THE MAGNETIC KEYS TO MASSIVE STAR FORMATION: THE WESTERN η CARINAE GIANT MOLECULAR CLOUD

PETER J. BARNES¹, STUART D. RYDER^{2,3}, GILES NOVAK^{4,5}, AND LAURA M. FISSEL⁶

¹Space Science Institute, 4765 Walnut St. Suite B, Boulder, CO 80301, USA

²School of Mathematical & Physical Sciences, Macquarie University, NSW 2109, Australia

³Astrophysics and Space Technologies Research Centre, Macquarie University, NSW 2109, Australia

⁴Center for Interdisciplinary Exploration & Research in Astrophysics, 1800 Sherman Ave., Evanston, IL 60201, USA

⁵Dept. of Physics and Astronomy, Northwestern University, 2145 Sheridan Rd., Evanston, IL 60208, USA and

⁶Dept. of Physics, Engineering Physics & Astronomy, Queen's University, 64 Bader Lane, Kingston, ON, K7L 3N6, Canada

Draft version April 28, 2025

ABSTRACT

We present SOFIA/HAWC+ continuum polarisation data on the magnetic fields threading 17 pc-scale massive molecular clumps at the western end of the η Car GMC (Region 9 of CHaMP, representing all stages of star formation from pre-stellar to dispersing via feedback), revealing important details about the field morphology and role in the gas structures of this clump sample.

We performed Davis-Chandrasekhar-Fermi and Histogram of Relative Orientation analyses tracing column densities $25.0 < \log(N/\text{m}^{-2}) < 27.2$. With HRO, magnetic fields change from mostly parallel to column density structures to mostly perpendicular at a threshold $N_{\text{crit}} = (3.7 \pm 0.6) \times 10^{26} \text{ m}^{-2}$, indicating that gravitational forces exceed magnetic forces above this value. The same analysis in 10 individual clumps gives similar results, with the same clear trend in field alignments and a threshold $N_{\text{crit}} = (1.9_{-0.8}^{+1.5}) \times 10^{26} \text{ m}^{-2}$. In the other 7 clumps, the alignment trend with N is much flatter or even reversed, inconsistent with the usual HRO pattern. Instead, these clumps' fields reflect external environmental forces, such as from the nearby HII region NGC 3324.

DCF analysis reveals field strengths somewhat higher than typical of nearby clouds, with the Bn data lying mostly above the Crutcher (2012) relation. The mass:flux ratio λ across all clumps has a gaussian distribution, with $\log \lambda_{\text{DCF}} = -0.75 \pm 0.45$ (mean $\pm \sigma$): only small areas are dominated by gravity. However, a significant trend of rising $\log \lambda$ with falling T_{dust} parallels Pitts et al. (2019)'s result: T_{dust} falls as N_{H_2} rises towards clump centres. In this massive clump sample, magnetic fields provide enough support against gravity to explain their overall low star formation rate.

Keywords: ISM: magnetic fields — stars: formation — ISM: kinematics and dynamics

1. INTRODUCTION

Magnetic fields (hereafter B fields) likely play an important role in the evolution of the interstellar medium (ISM). Particularly in molecular clouds where stars form, the impact of B fields is a long-standing question (McKee & Ostriker 2007; Crutcher 2012), stimulated further in the last few years by new models and data. Far-IR instruments (e.g., *Planck*, SOFIA's HAWC+ camera, BLAST-pol) have made sensitive, higher resolution, and/or wide-field maps of the plane-of-sky component B_{\perp} via linear polarisation measurements (e.g., Planck Collaboration 2016). Polarised radiation is thought to arise from non-spherical dust grains being oriented by radiative alignment torques (RAT) to the B field. While not all possible alignment mechanisms are magnetic, non-magnetic mechanisms are probably not dominant (Lazarian 2007).

Observationally, B field measurements rely on accurate values for the polarised contributions to emission or absorption (i.e., the Stokes parameters Q , U , V), which are usually much weaker than the total intensity I ; and then interpreting the data in terms of particular physi-

cal polarisation mechanisms, whether from alignment of dust grains or atomic/molecular effects (Zeeman, etc.), as explained by Crutcher (2012) or Barnes et al. (2015). This is compounded by challenges of making high-quality Stokes measurements in large cloud samples at high spatial dynamic range (SDR), and relating these to the clouds' other physical conditions.

If the dust polarisation alignment is magnetic, statistical methods can convert turbulent variations in field orientation $\theta_{B_{\perp}}$ to estimates of $|B_{\perp}|$ (Davis 1951; Chandrasekhar & Fermi 1953, hereafter DCF). Another analysis method, the histogram of relative orientations (HRO), compares the B_{\perp} field alignment to the orientation of dense gas structures to infer the threshold density n_0 where gravity appears to dominate B field pressure support (Fissel et al. 2016; Soler et al. 2017; Lazarian et al. 2018). Although approximate, both methods have been effectively used from cloud (10 pc) to core (0.1 pc) scales to meaningfully constrain the importance of B fields in different situations (Myers & Goodman 1991; Barnes et al. 2015; Fissel et al. 2019; Pattle et al. 2022; Barnes et al. 2023).

Studies using the Zeeman effect, which measures the

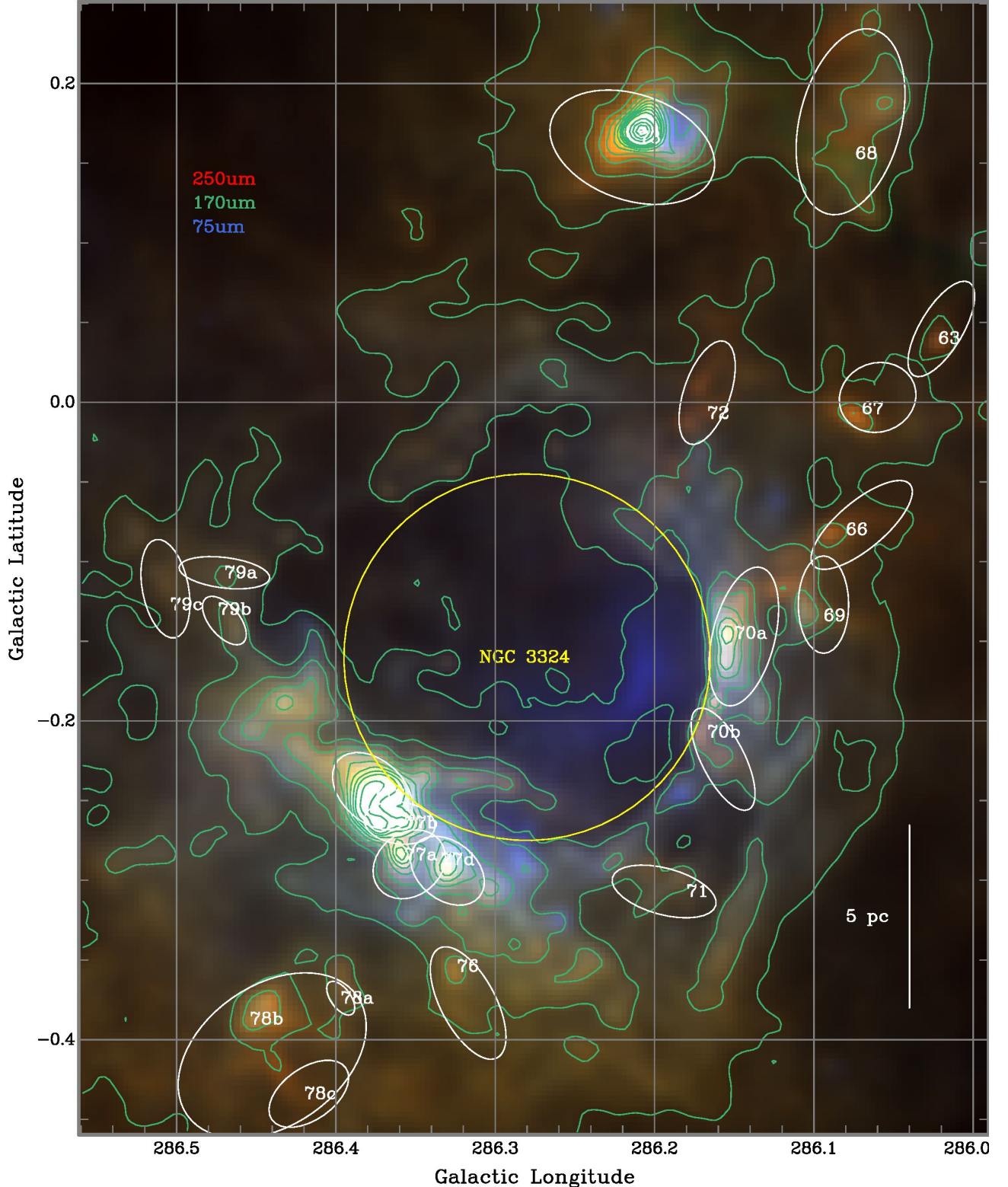


Figure 1. Composite RGB image as labelled from *Herschel*-PACS and -SPIRE data of the western end of the η Car GMC (Pitts et al. 2019). This shows the general molecular cloud cartography in a roughly 0.7×0.5 area surrounding the classic HII region NGC 3324 at a distance of 2.5 kpc (Samson 2021, giving the scale bar as shown) and encompassing most of Region 9 from the CHaMP project (Barnes et al. 2018). The FIR colour contrast was maximised in order to make clear the variations corresponding to the SED-fitted dust temperature T_{dust} : redder colours indicate cooler dust $\lesssim 10$ K where the $250 \mu\text{m}$ emission is more dominant, bluer colours show warmer dust up to ~ 40 K where $75 \mu\text{m}$ emission dominates. All the images are somewhat saturated for the brightest clumps in order to bring out details of the fainter FIR emission. Green contours are overlaid for the PACS $170 \mu\text{m}$ data at levels of 15(15)135 and 160(100)560 mJy/arcsec^2 , where $x(y)z$ denotes “from x in steps of y to z ”. Also overlaid as white ellipses are the approximate half-power sizes of the CHaMP clumps’ ^{12}CO emission (Barnes et al. 2016), each labelled by their BYF number at the ^{12}CO emission peak.

line-of-sight component of the field B_{\parallel} , have shown that below $n_0 \approx 300 \text{ cm}^{-3}$, B fields can support gas against gravity and have fairly uniform strength. Above this level, the line-of-sight component increases with density, $B_{\parallel} \propto n^{\kappa}$ where $\kappa = 0.65$, and the ratio of magnetic to gravitational forces is close to critical (Crutcher 2012). A more recent study by Whitworth et al. (2024) suggests that the change in slope κ at n_0 is more muted, and that n_0 itself is larger. Tracking local variations in the transition density n_0 and density dependence κ are both important to star formation (SF) theory, since SF is only observed in higher-density gas and a variable transition could change the SF efficiency and/or initial mass function.

Catching massive protostars in the act of formation, however, is more difficult than for low-mass protostars, because of their greater distances, accelerated timescales, and rapid alteration of initial conditions. Thus, data on massive cluster-scale clumps, where most massive protostars likely also form, are very sparse. We need to precisely measure both $|B|$ and n in a wider variety of clouds and environments to test these ideas.

Region 9 of CHaMP (the *Galactic Census of High- and Medium-mass Protostars*; Barnes et al. 2018) is a promising area for study, covering the western \sim third of the 120 pc-long η Carinae GMC (Fig. 1). It comprises 21 massive parsec-scale clumps across a 30 pc field, and includes the 9 pc-wide classic HII region/open cluster NGC 3324 at a distance of 2.50 ± 0.27 kpc (Samson 2021). These clumps (denoted individually by their catalogued BYF number from CHaMP; Barnes et al. 2011) form a representative sample of molecular clouds at all significant stages of star formation, from starless or pre-stellar (BYF 68, 71, 72, 76, 79a–c) to early-protostellar (BYF 63, 66, 67, 69, 78a–c) to more advanced massive protostellar stages (BYF 73, 77a–d) to post-SF feedback affected clumps (BYF 70a–b).

Importantly, all these clouds are physically and kinematically associated with each other at one distance, that of NGC 3324; see Pitts et al. (2019), Pitts & Barnes (2021), and references therein for information on a wide range of physical properties of these clouds. Intercomparing properties among *these* clouds avoids complications arising from samples at widely disparate distances observed with a single angular resolution. The project described herein was therefore conceived to examine, at a fixed physical resolution of 0.16 pc, the role of magnetic fields in star formation via polarisation mapping of this varied but representative sample.

Among these clumps, we have previously published observational studies of BYF 73 using SOFIA and other facilities. Pitts et al. (2018) reported SOFIA/FIFI-LS, *Gemini*, *Spitzer*, and ATCA data on the status of the most massive protostellar object in the cloud, MIR 2, and its less massive protostellar neighbours. Barnes et al. (2023) described SOFIA/HAWC+ and ALMA polarisation data on the cloud’s detailed physical conditions, including B fields, gas dynamics, and energetics. We now turn to the wider sample of clouds near BYF 73 in CHaMP Region 9, in order to put their overall and individual magnetic properties into a wider context.

In this paper, we describe the observational and data reduction procedures in §2. In §3 we use two standard

statistical methods to analyse our polarisation data and obtain constraints on the role of B fields in these clouds. We discuss all these results in §4 in order to highlight new insights from the data as well as their limitations. We present our conclusions in §5.

2. HAWC+ OBSERVATIONS AND DATA REDUCTION

This project was executed with HAWC+’s band D ($\lambda 154 \mu\text{m}$) filter in two stages, with first maps in Cycle 7 (one flight in July 2019)¹ of clumps BYF 73 and 77a–d, followed up by more extended mapping in Cycle 9 (four flights in July 2022)² of 11 more clumps. The project was also favourably reviewed for Cycle 10, but the sudden defunding of the observatory prevented us from completing the planned coverage of the other 5 clumps and achieving our overall sensitivity target.

During both Cycles we carefully planned to orient the fields at various position angles in the equatorial coordinate frame so as to optimise the camera’s coverage onto the brightest emission, and produce a relatively seamless mosaic. Unfortunately however, different software bugs in each Cycle prevented this optimisation during the observing runs, resulting in the fields being oriented in unexpected ways with respect to each other, as described further below.

The Cycle 7 mapping was done in the standard NMC nod-chop mode for that Cycle, which produces rectangular maps of angular size $\sim 4'$ corresponding approximately to the HAWC+ camera’s instantaneous sky footprint. Chopping and nodding were done asymmetrically due to the nearby FIR emission to the Galactic west and south. The total on-source integration times were 784.4 s for BYF 73 (1 field) and 1007.7 s for the BYF 77 complex (2 fields). Pipeline processing with HAWC-DRP produced final Level 4 quality Stokes image products which were downloaded from the SOFIA archive. This processing produces data that has all known instrumental and atmospheric effects removed, giving an absolute Stokes I calibration uncertainty of 20%, a relative polarisation uncertainty of 0.3% in flux and 3° in angle, and astrometry which should be accurate to better than $3''$ (Harper et al. 2018). However, we found the HAWC+ L4 astrometry for BYF 73 was still consistently offset $\sim 2''$ to the Galactic south compared to the other maps described by Barnes et al. (2023). Similarly, we found that the BYF 77 map was offset $\sim 4''$ to the Galactic south compared to the *Herschel* $70 \mu\text{m}$ map. We inserted both of these corrections by hand into the HAWC+ data files.

The Cycle 9 mapping utilised the newly-available on-the-fly (OTF) mode, in order to improve the observing efficiency & sensitivity and produce slightly larger ($\sim 6'$) & more-easily mergeable fields, albeit with a somewhat variable noise level across each field due to the integrated sky coverage of the camera using a Lissajous scanning

¹ See the HAWC+ description at <https://irsa.ipac.caltech.edu/d/ata/SOFIA/docs/instruments/hawc>, its Data Handbook at https://irsa.ipac.caltech.edu/data/SOFIA/docs/instruments/handbooks/HAWC_Handbook_for_Archive_Users_Ver1.0.pdf, and the Cycle 7 Observer’s Handbook at <https://irsa.ipac.caltech.edu/data/SOFIA/docs/sites/default/files/Other/Documents/OH-Cycle7.pdf> for details of the observing modes.

² See the Cycle 9 Observer’s Handbook at <https://irsa.ipac.caltech.edu/data/SOFIA/docs/sites/default/files/2022-12/oh-cycl9.pdf> for details of the observing modes.

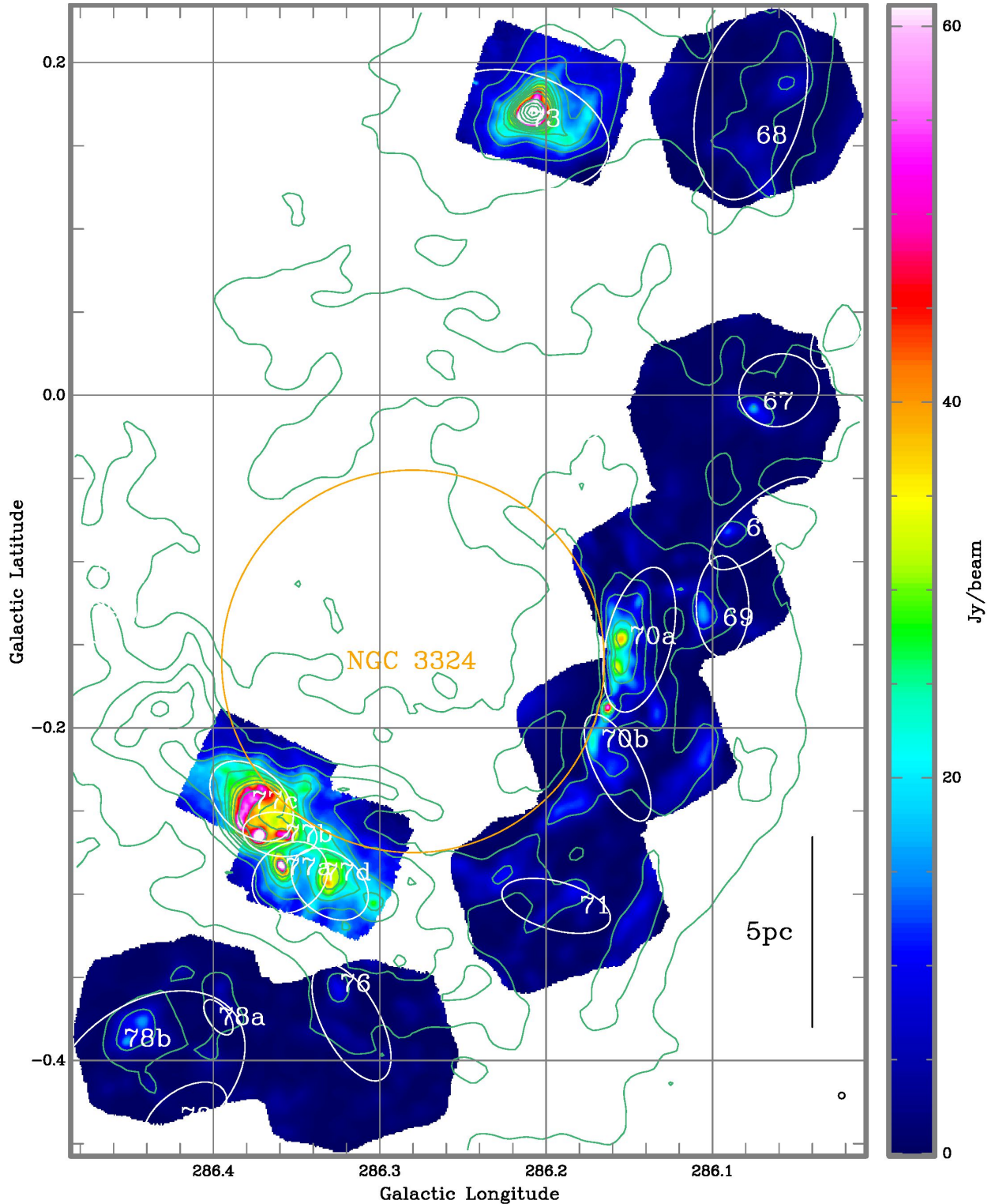


Figure 2. Overview of all SOFIA HAWC+ band D ($154\mu\text{m}$) total intensity (Stokes I) maps of Region 9 from both Cycle 7 (2019) and Cycle 9 (2022) observations, covering almost the same area as Fig. 1. The band D angular resolution, $13''/6$, is shown in the bottom right corner as a very small black circle. The three Cycle 7 fields show up as smallish rectangles, reflecting the instantaneous field of view of the HAWC+ camera and the standard nod-chop (NMC) imaging procedure with fixed blank-sky reference locations. The seven Cycle 9 fields appear as slightly larger irregular octagons, reflecting the coverage of Lissajous tracks on the sky for the more efficient on-the-fly (OTF) imaging procedure available then. The I image is overlaid by the same white ^{12}CO ellipses and green PACS contours as in Fig. 1; the latter can be converted to the HAWC+ data scale by a factor $210\text{arcsec}^2/\text{bm}$, and both instruments' maps are seen to conform well to each other. The peak I intensity is highly variable across the different clumps visible here. Compact sources in BYF 73 (north of NGC 3324) and 77 (on the SE edge of NGC 3324) reach peak flux densities of 478 and 90Jy/bm (respectively) and so are saturated on the displayed I scale (colour bar on the right), but the extended emission under 60Jy/bm is well-reflected in the image. In either observing mode, the typical rms I error in the interior of each field has a central minimum around $0.10\text{--}0.13\text{Jy/bm}$, rising to $2\text{--}5\times$ these values around the field boundaries; the S/N in the various emission features then runs from a few 100s to >5000 .

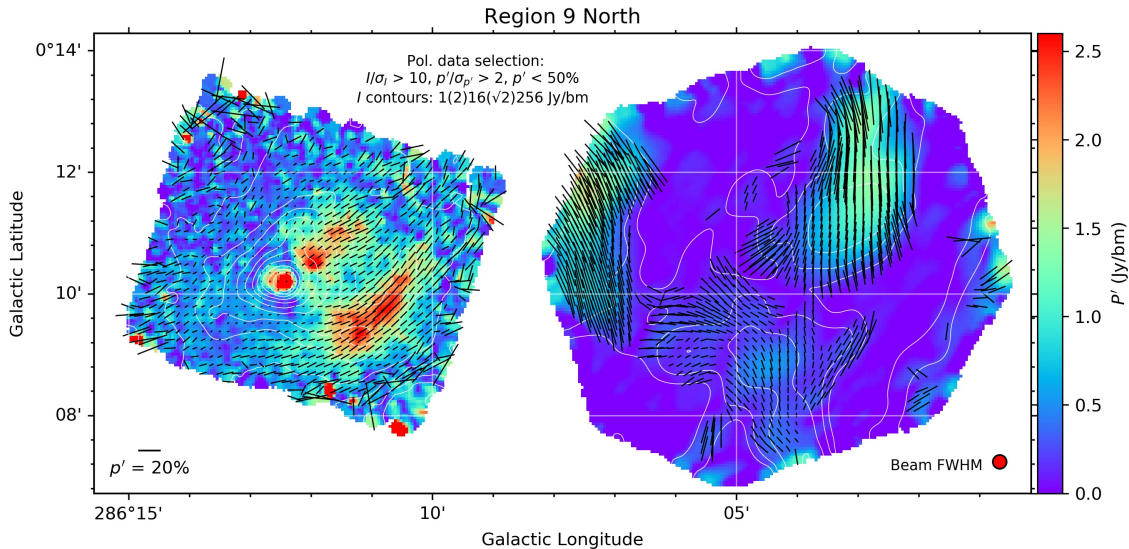


Figure 3. Zoom in to the northern portion of Fig. 2 showing fields for the clumps BYF 73 (left) and 68 (right). The background image is now the HAWC+ debiased polarised flux density P' , overlaid here by white HAWC+ I contours as labelled. At every 3rd pixel (0.6 beam) satisfying the indicated selection criteria, we also display black “vectors” showing the debiased polarisation percentage (p' , with a scale bar shown in the bottom left corner) at a position angle (with the usual $\pm\pi$ degeneracy) of the plane-of-sky B field component (i.e., rotated 90° from the observed polarisation direction). The respective BYF 73/68 peak P' values are 5.2/1.7 Jy/bm, with central uncertainties 0.12/0.05 Jy/bm rising slowly to each field’s edge, and S/N peaking at 33/20. The percentage polarisation p' has very similar S/N to P' , while uncertainties in the position angle/inferred B field orientation are typically a few degrees, except for the noisier pixels at the edge of the BYF 73 field. Consult Fig. 6 to see how the polarisation data quality varies across all the HAWC+ fields.

pattern. The total on-source integration time across the 7 OTF fields was 3388 s for an average of 484 s per field. In addition to the normal calibrations as above, all 7 fields were merged in the HAWC-DRP to produce the final L4 Stokes mosaics. The astrometry in this case was found to be internally consistent across the mosaic, but offset by $\sim 3''$ to the Galactic west compared to the *Herschel* $70\ \mu\text{m}$ map, a correction for which was again inserted by hand.

For the data analysis described in the following sections, the Level 4 data for all fields from both Cycles were mosaicked together onto a consistent J2000 equatorial grid for each Stokes parameter using the MIRIAD package (Sault et al. 1995) in a set of custom unix shellscripts, then transformed to Galactic coordinates to simplify comparisons with other data. Supplementary analysis and display also included use of Jupyter notebooks from sample python scripts in the online HAWC+ handbooks, the *karma* package (Gooch 1997), and the SuperMongo package (Lupton & Monger 2000).

3. DATA ANALYSIS

At a distance of 2.50 ± 0.27 kpc for NGC 3324 (Samson 2021), the scale in Region 9 is $36'' = 0.44$ pc, or 0.1 pc = $8''.25$. Thus, HAWC+ band D gives us a useful spatial dynamic range from 0.08 pc to the maximum scale in the mosaic, ~ 30 pc, a linear factor of about 360 and exceeding 10^4 resolution elements in area.

The final Stokes I mosaic is shown in Figure 2, overlaid with the same features as in Figure 1. Poor overlaps of adjacent fields due to the observing software PA bugs, especially for the Cycle 9 data, are also visible.

To display the details of the HAWC+ polarisation data more clearly, we show zoomed-in displays of the northern (Fig. 3), western (Fig. 4), and southern (Fig. 5) HAWC+ fields, all on a common printed scale. In each field, the background image is the debiased Stokes P' , overlaid by white contours of the Stokes I (the same data as the

Fig. 2 background image) plus “vectors” of the debiased polarisation percentage p' . These data products can be directly analysed by standard techniques.

A summary plot of the data quality is given in Figure 6. The fraction of pixels with polarisation S/N above any quality level goes up as the HAWC+ I flux rises. For example, at $I \gtrsim 2.5$ Jy bm^{-1} (slightly lower than the lowest PACS contour in Figs. 1 and 2), $>50\%$ of the polarisation data points have S/N >3 in p' . At $I \gtrsim 15$ Jy bm^{-1} , $>80\%$ of the vectors have S/N >3 and $>50\%$ have S/N >5 . Allowing for the oversampling of the HAWC+ beam in Figs. 3–5, there are roughly 9,000 independent polarisation measurements with S/N >3 in the combined Cycle 7+9 data sets.

In what follows, we use the same general analysis approach (DCF and HRO methods) as for our prior detailed BYF 73 study (Barnes et al. 2023). This will facilitate comparisons in the respective results.

3.1. Davis-Chandrasekhar-Fermi (DCF) Method

DCF analysis (Davis 1951; Chandrasekhar & Fermi 1953) is a widely-used approach that yields B field estimates from plane-of-sky polarisation data; however, it is rather approximate (see reviews by Crutcher 2012; Liu et al. 2022). Its appeal is to directly link the dispersions in polarisation angle $\delta\theta = s$ (tracing variations in the B field orientation) to physical parameters in the ISM, assuming that s arises from the propagation of a transverse MHD wave in a turbulent plasma. The degree to which this is true gives rise to the uncertainties.

Under this assumption, the dispersion s is related to three other physical parameters that simply and naturally describe the MHD wave: the gas density n , the line-of-sight velocity dispersion δV , and the plane-of-sky magnetic field strength B_\perp . That is, s will increase as (1) B decreases, since then the magnetic restoring forces are reduced; (2) n increases, since then the medium’s in-

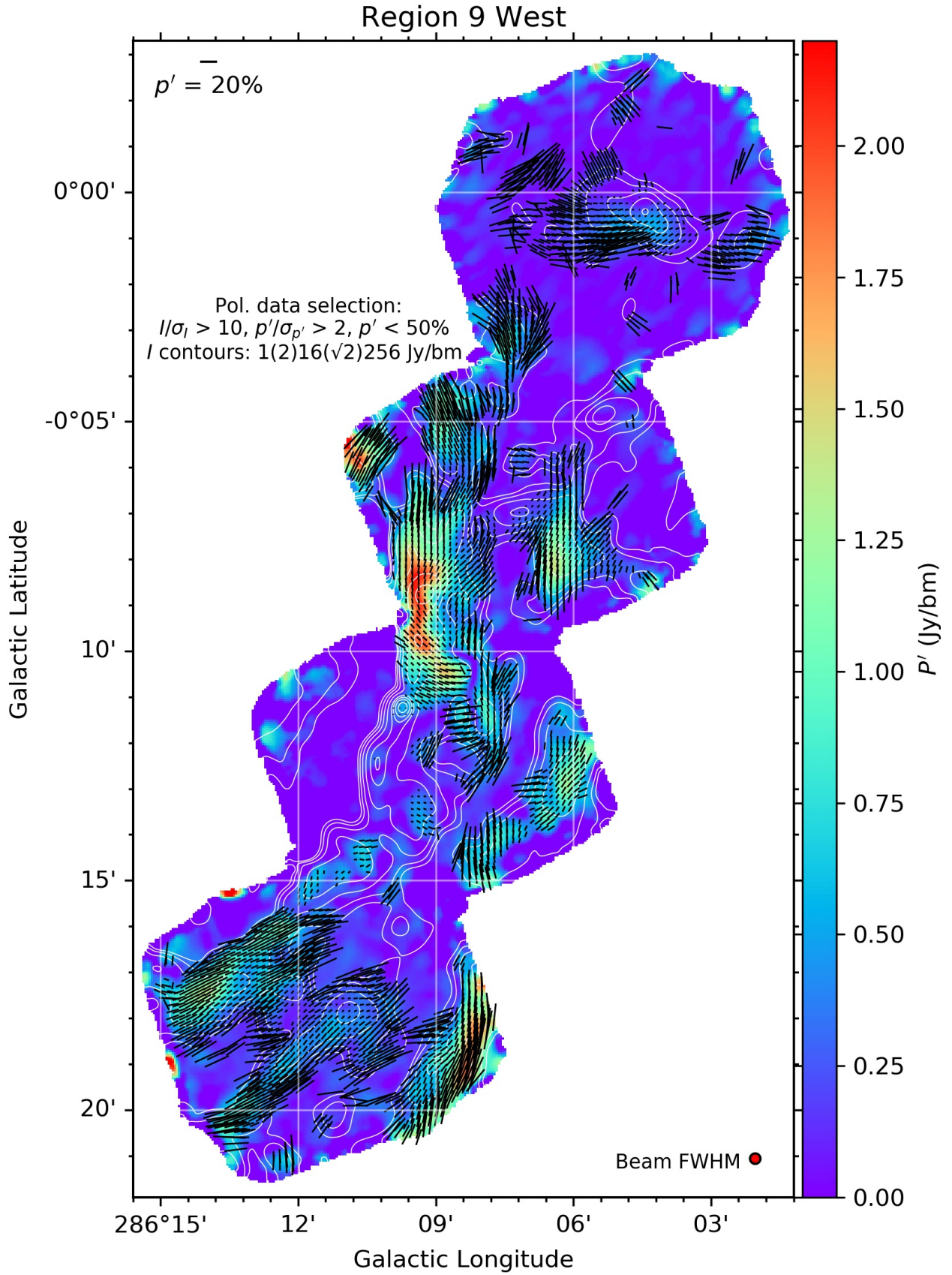


Figure 4. Similar zoom in to Fig. 3 but here for the western portion of Region 9 (clumps BYF 66, 67, 69, 70a–b, and 71). The background image is again of P' with a peak of 2.2 Jy/bm, uncertainty minima 0.03, 0.06, 0.10, and 0.06 Jy/bm in the 4 fields from north to south, and peak S/N of 18. The vector selection criteria are as before.

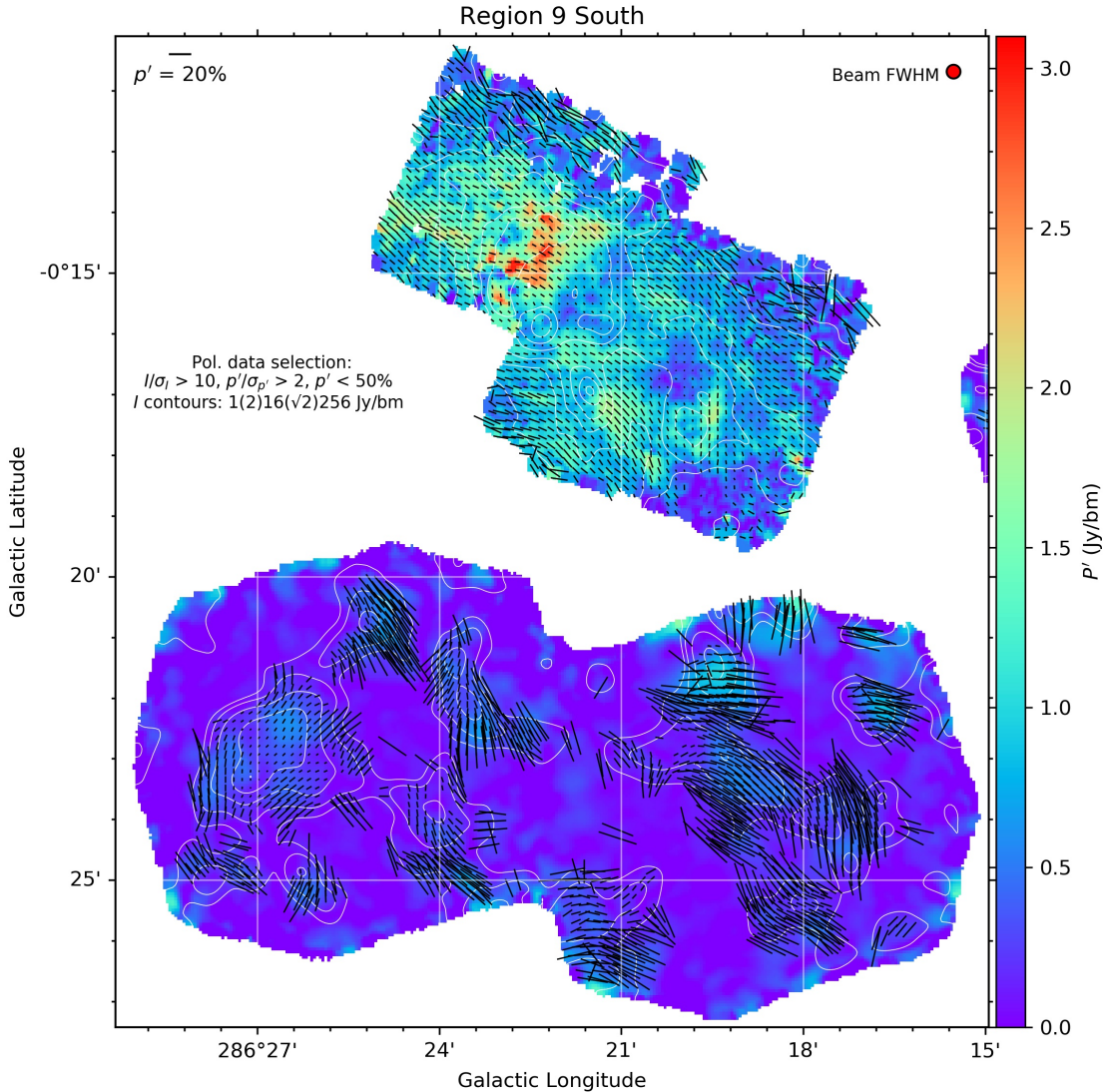


Figure 5. Zoom in to the southern portion of Region 9 (clumps BYF 76, 77a–d, and 78a–c). The background P' image has a peak of 3.1 Jy/bm, uncertainty minima $\sim 0.2, 0.08, 0.05,$ & 0.04 Jy/bm in the 4 fields from top-left to bottom-right, and peak S/N of 26. The vector selection criteria are as before.

ertia to the MHD wave is greater; or (3) δV increases, since that describes the strength of the MHD wave.

Following Barnes et al. (2015), we use the SI formulation ($1 \text{ nT} = 10 \mu\text{G}$) of the DCF relation:

$$B_{\perp, \text{DCF}} = 0.558 \text{ pT} \sqrt{\mu n} (\Delta V/s), \quad (1)$$

where n (m^{-3}) is the gas density with mean molecular weight $\mu=2.35$, $\Delta V = \sqrt{8 \ln 2} \delta V$ is the velocity FWHM (km s^{-1}) in the cloud, and s is measured in degrees. Included in the constant is a numerical factor $Q = 0.5$ from Crutcher et al. (2004) to correct for various smoothing effects (e.g., see Ostriker et al. 2001), although recent work summarised by Liu et al. (2022) suggests Q can vary somewhat (~ 0.3 – 0.6) in various circumstances.

However, several modifications to the classical DCF method have also been proposed (see Pattle et al. 2022). Among these is that of Skalidis & Tassis (2021), who point out that the original DCF approach was for incompressible Alfvén waves; according to them, compressible MHD waves should dominate in the ISM. They propose

$$B_{\perp, \text{ST}} = 0.1042 \text{ pT} \sqrt{\mu n/s} (\Delta V), \quad (2)$$

where we have converted their relation to the same SI units as Eq. (1). The general effect of Eq. (2) is to give, with the same inputs, slightly smaller B_{\perp} values than the classical DCF method. Other alternatives have also been proposed, as described by Pattle et al. (2022), but the differences are subtle, and we are content to consider the above two approaches as representative.

Either way, with estimates, or even better, *maps* of the quantities n , ΔV , and s , we can compute maps of the estimated line-of-sight component B_{\perp} (subject to the uncertainties that go into Eqs. 1 and 2).

We start by deriving s maps from our HAWC+ data. The somewhat involved procedure is described in [Appendix A](#); the final result is shown in [Appendix B](#).

We next consider the density. We can't measure n directly, but estimate it instead from two other parameters. These are: (1) the N_{H_2} from SED fitting of *Herschel* data (shown as green contours in Figs. 7–10, from Pitts et al. 2019), which is likely the best type of estimate for the total gas column density in the cold ISM; and (2) a simple but appropriate estimate for the (*a priori* unknown) line-of-sight depth R of the clumps across Region 9, to

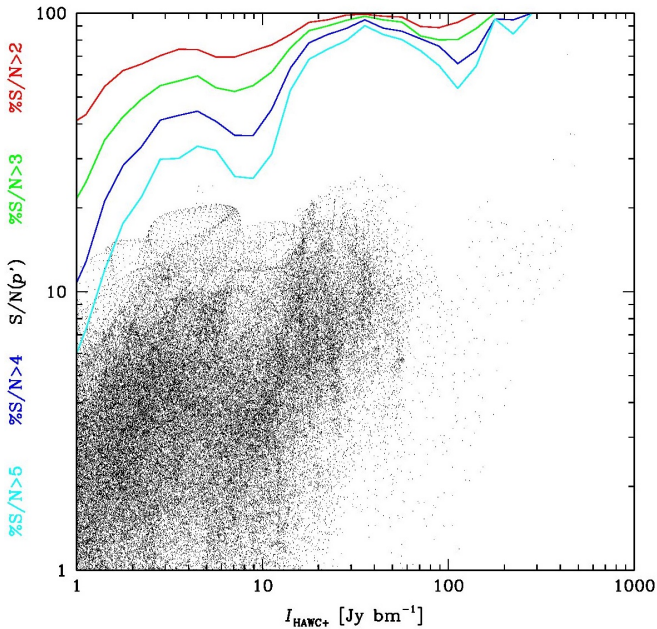


Figure 6. Summary of data quality metrics for all polarisation vectors shown in Figs. 3–5. The data points show the S/N in p' at each pixel as a function of the pixel’s HAWC+ I flux (black axis labels). The maximum S/N is 37, and the y-scale goes down to S/N = 1 for simplicity. The coloured lines and coloured y-axis labels show the fraction of these points, as a percentage, that have S/N > the indicated values as a function of I .

convert from column to volume density.

We could use various structure-finding approaches to evaluate the sizes of the more obvious clumps in the FIR or spectral-line data (such as the Mopra ellipses displayed in these figures), and then assume depths for these structures commensurate with their projected sizes. But this approach is somewhat unsatisfying, since it uses only some of the structural information available in the maps. We choose instead an estimate for R which is structure-agnostic.

Consider the gradient ∇N_{H_2} of the column density map. Molecular clouds have structure on scales all the way from a map’s size to the resolution limit, often with local maxima embedded in the more extended structure. Thus, gradients like ∇N_{H_2} generally indicate where values rise towards each local peak. Given this, an appropriate size scale or depth for the more extended cloud envelope will be larger than the \sim beam-sized scale/depth for the smaller structures. In other words, the shallower the gradient, the larger the size and inferred depth. Conversely, the steeper the gradient, the smaller the size/depth. So, we initially estimate the appropriate depth across our maps as the inverse of the relative gradient (hereafter, IRG) in the N_{H_2} map, i.e., $N_{H_2}/\nabla N_{H_2} = \text{IRG} = R$ (with the relevant unit conversions).

However, this estimate will tend to fail where the gradient, assumed to be smoothly increasing towards each isolated clump peak, becomes very small around local maxima, since a very small ∇N_{H_2} means a very large R , making the derived density very small. Away from the actual clump peaks this is of little consequence, since there, the derived densities are already small (and there is less likelihood of polarisation data anyway). But near the smaller clump peaks where N reaches significant maxima and the polarisation S/N is also optimal, the gradients will systematically approach zero, leading to very large

R and very small n , just where we expect n to peak. This appears as prominent, unphysical “doughnut holes” in the n maps at the N peaks.

To cure this, we also compute the Laplacian (i.e., curvature) of the column density map, $\nabla^2 N_{H_2}$, which would be positive everywhere that the gradient keep increasing. Where the gradient decreases — and especially around significant peaks, goes to zero — the Laplacian becomes negative. Where this happens, we use this threshold as a discriminant to substitute a maximum R scale for the IRG, namely the projected beamsize. The resulting maps for R & n appear in Appendix B.

In summary, we use

$$\begin{aligned} n &= \frac{N_{H_2}}{R} = \frac{N_{H_2}}{\text{IRG}} = \frac{N_{H_2}}{N_{H_2}/\nabla N_{H_2}} \\ &= \nabla N_{H_2}, \quad \text{where } \nabla^2 N_{H_2} > 0 \\ &= N_{H_2}/R_{\text{beam}}, \quad \text{where } \nabla^2 N_{H_2} \leq 0. \end{aligned} \quad (3)$$

Finally, we need a velocity dispersion map to compute the DCF-based B_{\perp} . We take the $N_{12\text{CO}}$ -derived σ_V for Region 9 from Barnes et al. (2018), which has the advantage over any single-species σ_V (such as from ^{12}CO or ^{13}CO) of being intrinsically corrected for the line opacity in either species (see Appx. B). Combining these maps of s , n , and ΔV according to Eq. (1), we show maps of B_{\perp} in Figures 7a–10a.

Having computed a map of B_{\perp} , we can add another important data product as a bonus. As a measure of the relative importance of gravity (compression of clumps or cores) to B fields (pressure support), the mass-to-flux ratio M/Φ has been widely used to highlight structures that are susceptible or resistant to star formation (e.g., Crutcher et al. 2004). From Barnes et al. (2015) we can write

$$\lambda = \frac{(M/\Phi)_{\text{obs}}}{(M/\Phi)_{\text{crit}}} = 6.38 \frac{N_{H_2}/10^{26}\text{m}^{-2}}{B_{\text{TOT}}/n\text{T}} \quad (4)$$

and assume that $B_{\text{TOT}} = 2B_{\perp, \text{DCF}}$ on average. Then, wherever $\lambda \gg 1$ (or equivalently, $\log_{10}\lambda \gtrsim 0.5$), gravitational forces are stronger than magnetic forces and the likelihood of SF is enhanced; such a structure is considered to be “supercritical.” Conversely, where $\lambda \ll 1$ (or $\log_{10}\lambda \lesssim -0.5$), SF is inhibited (subcritical); $\lambda=1$ suggests that these forces are close to equilibrium. Thus, a map of λ can be compared to other tracers and provide useful insights into the dominant processes in a given cloud. With the B and N maps already in hand, we get the $\log_{10}\lambda$ maps shown in Figures 7b–10b.

These $\log\lambda$ maps are suggestive in places, but not necessarily definitive. For example, in the North (Fig. 7), the massive collapsing core MIR 2 in BYF 73 (a known massive YSO; Barnes et al. 2023) is surrounded by a dense core with $\log\lambda$ systematically >0.2 , as one might expect where apparently gravitationally-driven inflows are overwhelming any means of support. Meanwhile, the cloud’s adjacent compact HII region transitions sharply to $\log\lambda < -0.7$, again as expected for an overpressured bubble. Nearby to the west, the quiescent, cold, starless clump BYF 68 has the strongest B field measured in Region 9. Its $\log\lambda$ is <-0.5 almost everywhere across it, except for a small patch peaking around 0.1, consistent with the B field alone being capable of preventing most SF.

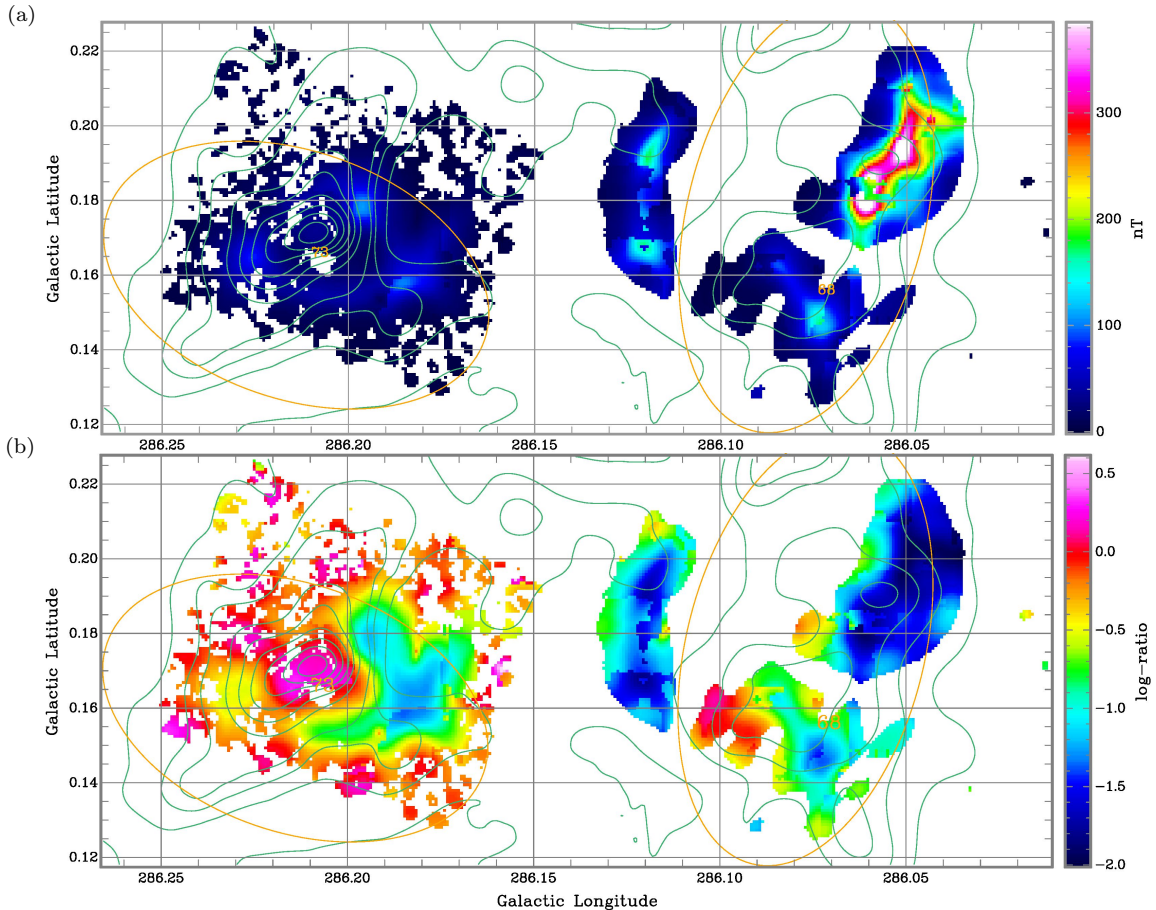


Figure 7. Maps of (a) B_{\perp} from DCF computation of Eq. (1), and (b) $\log_{10}\lambda$ from Eq. (4), in Region 9 North. Clump sizes of BYF 73 and 68 are shown by ellipses as in Figs. 1 and 2, while contours are of column density N_{H_2} from Pitts et al. (2019), at levels $0.5(0.5)^2$ and $4(2)14 \times 10^{26}$ molecules m^{-2} . In (a), the colour scale is slightly saturated to show weaker B_{\perp} features; the peak B_{\perp} value in BYF 68 is 469 nT. In (b), the colour scale spans the full range of $\log\lambda$ values.

In the West and South subregions, the B fields are somewhat strong in places, but otherwise rather moderate (i.e., $\sim 50\text{--}200$ nT). Reflecting this, the $\log\lambda$ values are generally somewhat negative. The largest patches that approach or exceed $\log\lambda = 0.2$ are on the edges of BYF 67 (~ 0.1) and 76 (~ 0.3). Even where some YSOs are evident (BYF 70a, 77ab), $\log\lambda$ is still < 0 , and one is left to speculate that SF is only being triggered in these clouds because of the strong feedback from NGC 3324.

Overall in Region 9, the $\log\lambda$ distribution is very close to gaussian, with a very small extra tail to positive values (see §4). The mean \pm sigma values are $\log\lambda = -0.75 \pm 0.45$. Above the 2σ level ($\log\lambda > 0.15$) we find 2.2% of the pixels; above 3σ ($\log\lambda > 0.6$), we find 0.22%. Both fractions are about 50% higher than expected for a truly gaussian tail. Thus in this sample, it is rare even for massive molecular clumps to be supercritical, but the exceptions to this may be important — see §4 for more details.

3.2. Histogram of Relative Orientations (HRO)

In this section we similarly follow our prior analysis procedures for BYF 73 (Barnes et al. 2023).

The HRO method of analysing B field orientations in star-forming gas is another widely-used, standard technique (e.g., Soler et al. 2017, and references therein). It allows us to examine how the B field orientation changes with column density. Usually, at lower molecular gas column densities $\sim 10^{26}$ m^{-2} , the B field direction tends

to be mostly parallel, or not show any preferred direction, relative to gas structures. In contrast, the B field is mostly perpendicular to higher column density structures $\sim 10^{27}$ m^{-2} . This generally confirms a series of results by the lower resolution ($\sim 10'$) Planck Collaboration (Planck Collaboration 2016) over a wider range of molecular gas column densities.

This is widely attributed to a transition from subcritical gas at lower densities, where the flow is at least guided to some extent by the B field, to near-critical or slightly supercritical gas at higher densities, where gravity is capable of overwhelming the magnetic pressure, allowing stars to form. Does Region 9 conform to this picture?

We show first in Figure 11 the per-pixel relative alignment of B field vectors for all the HAWC+ data in Figures 3–5, stratified by the SED-fit column density N (Pitts et al. 2019) which we use as a proxy for “structure” in the molecular gas. That is, where the rotated polarisation vectors $\theta_{B_{\perp}}$ are aligned with the tangent to the iso- N contours, the relative angle is close to 0° and the field is considered to be “parallel” to the gas structures. Where $\theta_{B_{\perp}}$ is perpendicular to the contours and aligned with the column density gradient ∇N , the relative angle is close to 90° and the field is considered to be “perpendicular” to the gas structures.

This approach has the advantage of not imposing any preconceived interpretation of whether the gas structures represent “clumps,” “cores,” “filaments,” or any other po-

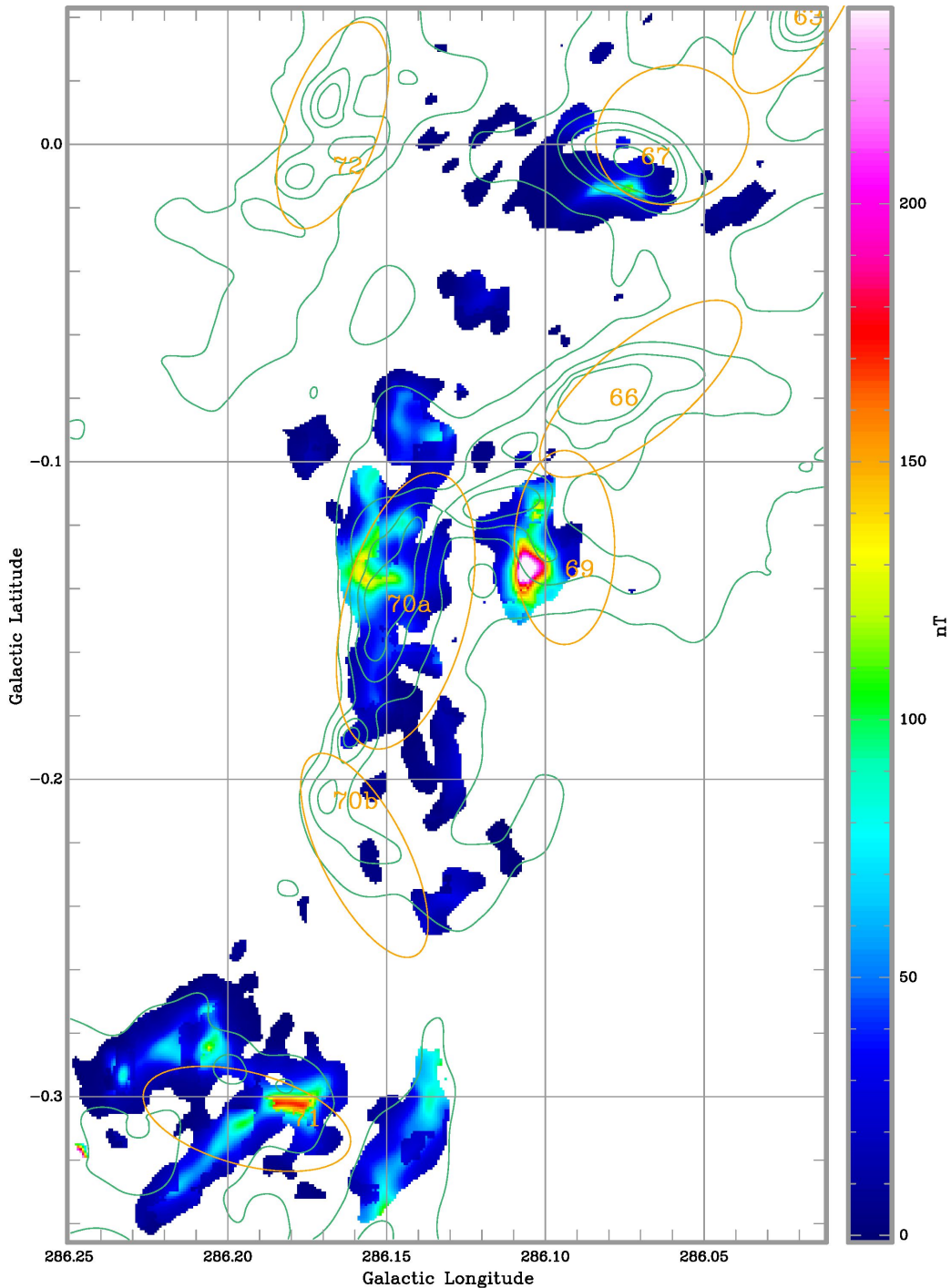


Figure 8. (a) Map of B_{\perp} as in Fig. 7a but for Region 9 West (BYF 66, 67, 69, 70a–b, 71). The printed scale is the same, as are the overlaid $N(\text{H}_2)$ contours and ^{12}CO ellipses. The colour scale is again slightly saturated; the peak B_{\perp} value in BYF 69 is 324 nT.

tentially subjective term (see Planck Collaboration 2016; Soler et al. 2017). The angle distribution is then quantified by computing histograms on each N -bin separately as in Figure 12, including the HRO shape parameter $-1 < \xi < 1$ computed on each N bin’s HRO, as described by Soler et al. (2017). This parameter objectively indicates whether there is a preponderance of parallel ($\xi > 0$) or perpendicular ($\xi < 0$) alignments in the data, and can be plotted as a function of N (Fig. 13) to reveal any trends via linear regression,

$$\xi = C_{\text{HRO}} (\log N - X_{\text{HRO}}). \quad (5)$$

Already in Figure 11 we can see that the distribution of relative alignments has definite patterns in various column density ranges. These observations are reflected numerically in Figures 12 and 13.

First, we discount the lowest N bin because those data have low S/N in the $\theta_{B_{\perp}}$ values, hence the relative PA distribution is not so reliable (uncertainties $\sim 20^\circ$ or more). But in the next 16 low- N bins, there is a strong overabundance of parallel alignments (relative PA $\lesssim 20\text{--}40^\circ$) between the inferred B field orientation $\theta_{B_{\perp}}$ and the iso- N contours. Not only do each of these 16 bins have their shape parameter $\xi > 0$ to high significance

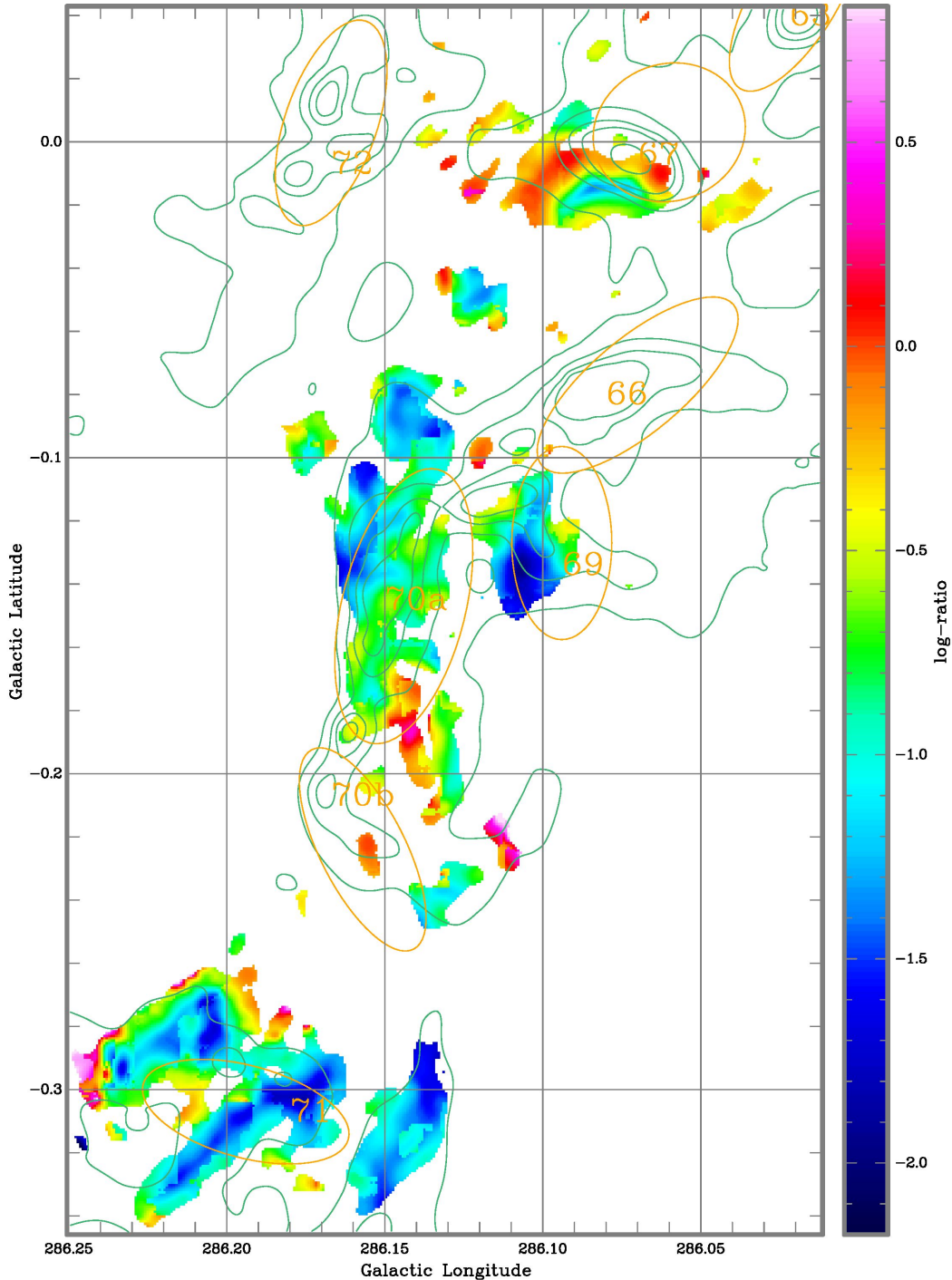


Figure 9. (b) Map of $\log_{10}\lambda$ as in Fig. 7b but for Region 9 West (BYF 66, 67, 69, 70a–b, 71). The printed scale is the same, as are the overlaid $N(\text{H}_2)$ contours and ^{12}CO ellipses. The colour scale spans the full range of $\log\lambda$ values.

(4–15 σ), but there is a strong downward trend in ξ as N rises. In the top three N ranges, the downward trend in ξ continues to ~ 0 , with PAs more broadly distributed (~ 20 – 60°) in those bins. Unlike the BYF 73-only plots, though, which included higher-resolution ALMA data and reached higher N in that clump, in Region 9 generally we do not clearly progress to a column density regime where the alignments are more perpendicular (i.e., $\xi < 0$ or, say, $\text{PA} \gtrsim 50^\circ$).

Nevertheless, the negative trend of ξ with N is clear, especially for the red fit in Fig. 13, with a slope $C_{\text{HRO}} =$

-0.51 . This is of similar magnitude and significance (8σ) to the BYF 73-only results (Barnes et al. 2023). Furthermore, the transition value of $\log N$, where ξ goes through 0 for Region 9 as a whole, is $X_{\text{HRO}} = 26.56$ (red value in Fig. 13), within 3σ of the BYF 73-only value as well (Barnes et al. 2023) and similarly sharp (small uncertainty). Thus, our HAWC+ data and HRO analysis suggest that we are possibly tracing a common relationship in these massive clumps between their B fields and their star-forming structure. We examine this idea in more detail next.

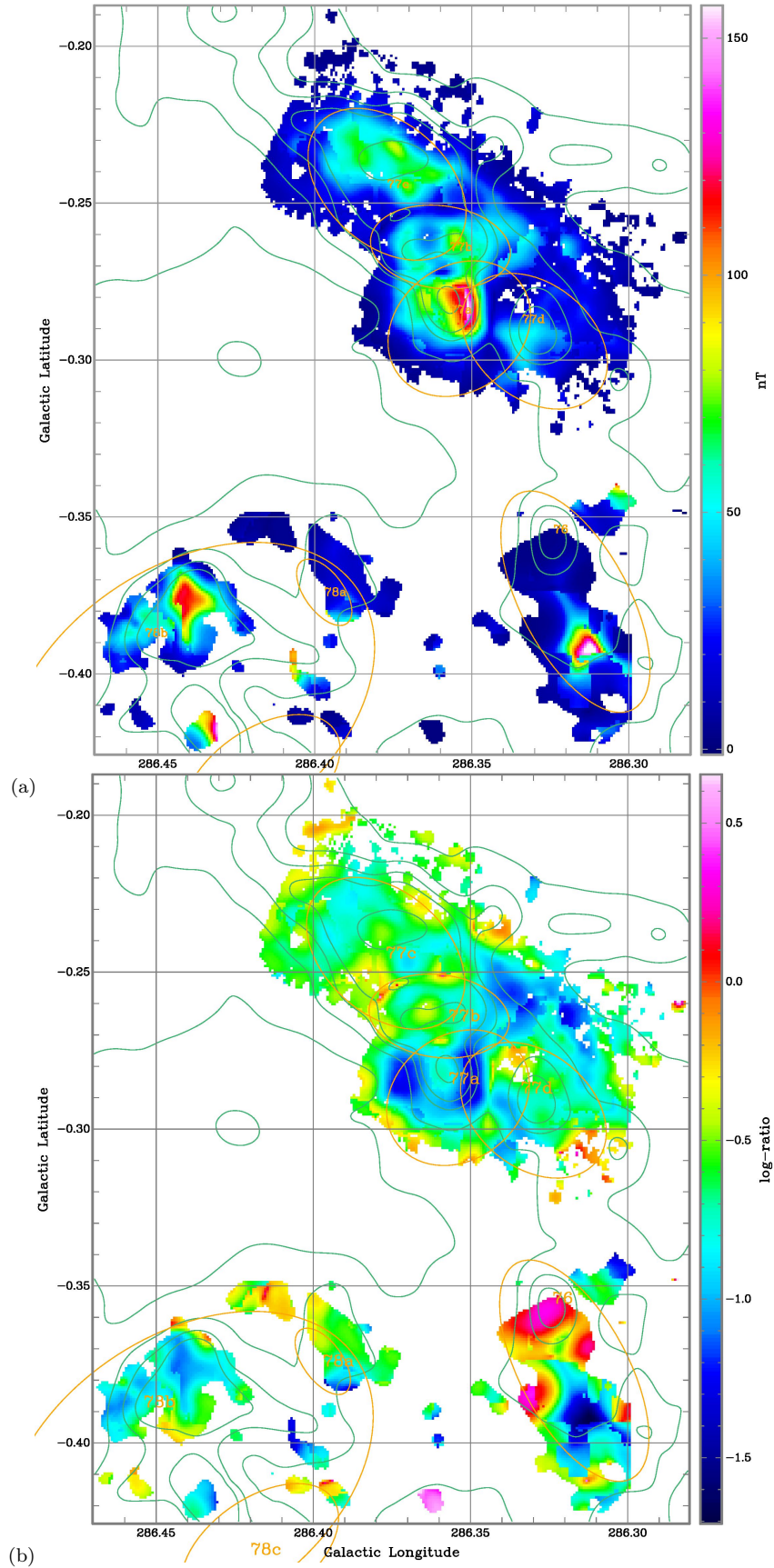


Figure 10. Maps of (a) B_{\perp} as in Figs. 7a & 8a, and (b) $\log_{10} \lambda$ as in Figs. 7b & 9b, but for Region 9 South (BYF 76, 77a–d, 78a–c). The printed scale is the same, as are the overlaid $N(\text{H}_2)$ contours and ^{12}CO ellipses. In (a), the colour scale is again slightly saturated; the peak B_{\perp} value in BYF 76 is 177 nT. In (b), the colour scale spans the full range of $\log \lambda$ values.

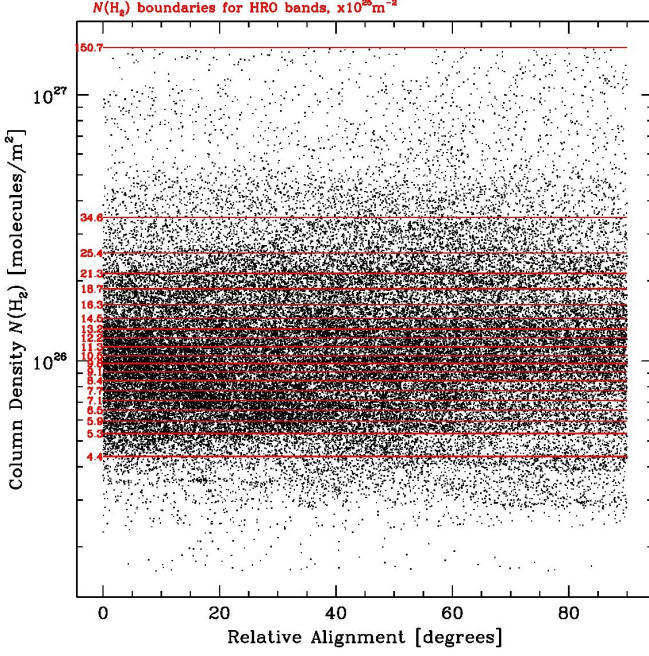


Figure 11. Relative alignment between polarization position angle $\theta_{B\perp}$ and the tangent to iso-column density N contours, as a function of N across the HAWC+ field. An angle of 0° means the B field is oriented along the iso- N contours, while at 90° the field is perpendicular to the contours and aligned with the gradient ∇N . Also shown as red lines and labelled in N , in units of 10^{25}m^{-2} , are the boundaries of the separate bands in N for which each histogram in Figure 12 was computed. The boundaries were chosen to ensure histogram equalisation, i.e., to divide all N data into 20 equally-populated bins with comparable statistical noise in each N -bin.

3.3. Comparison Among Region 9 Clumps, and with Other Studies

It is instructive to break down our HRO analysis by smaller areas, to see if these parameters are everywhere the same or if the above results are simply an average of some wider environmental effect(s). Indeed, having already defined the ROIs for the DCF analysis, we can re-use them for this purpose. The results for each are shown in Appendix C, and a summary plot of the trends appears in Figure 14.

Among these HRO ξ - N regression fits, we see that they clearly split into two groups plus 1 outlier. First, there are 10 ROIs with clearly-defined negative slopes C_{HRO} (average slope/error ~ 4) and $\log N$ intercepts covering a relatively narrow range ($X_{\text{HRO}} = 26.3 \pm 0.4$) with small individual $\log N$ uncertainties (average ≈ 0.13). This group is comprised of BYF 67, 68c, 68e, 68n, 71w, 73Hs, 76, 77abc, 77d, and 78b; we dub it the “nominal” group.

The fits for the other 7 ROIs are quite different, in that their slopes C are positive or flat but poorly-defined, and the X values vary widely with large uncertainties. Six of these have slopes C_{HRO} consistent with 0 (average slope/error ~ 1) and $\log N$ intercepts covering two orders of magnitude in N ($X_{\text{HRO}} = 26.4 \pm 1$) with large individual $\log N$ uncertainties (~ 0.5 – 12). We call this group of BYF 69, 70a, 70aS, 71, 73Hn, and 78a the “flat” group.

The last ROI, BYF 70aN, is an outlier from both the above groups, with a very large positive slope C_{HRO} (both the slope and slope/error are ~ 8) but unremarkable $\log N$ intercept ($X_{\text{HRO}} = 25.75$).

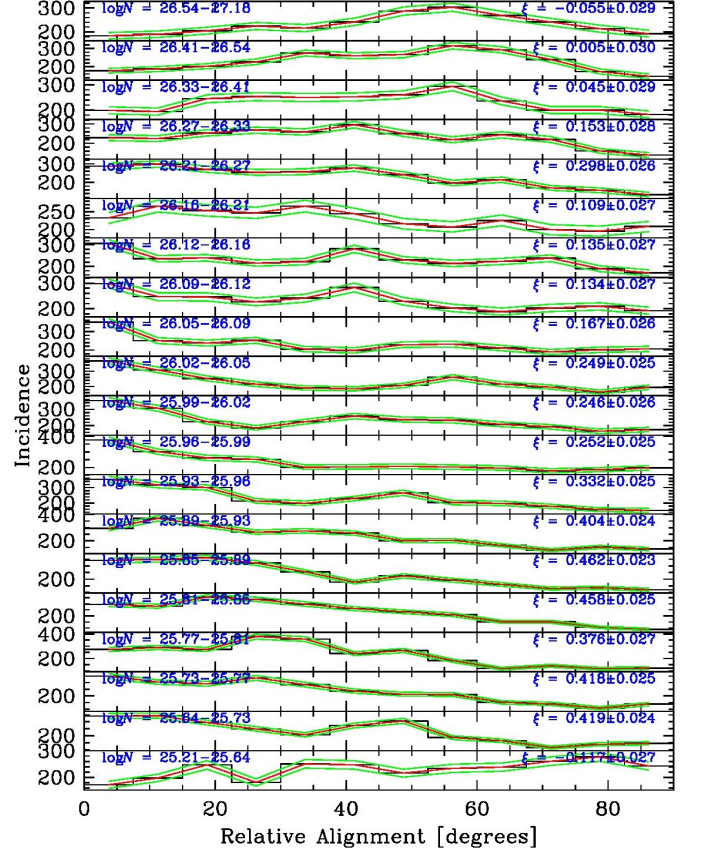


Figure 12. HRO plots in each of the N -bins shown in Figure 11. Each window is labelled by the range of column density N in that bin and its fitted HRO shape parameter $\xi \pm$ uncertainty, as defined by Soler et al. (2017).

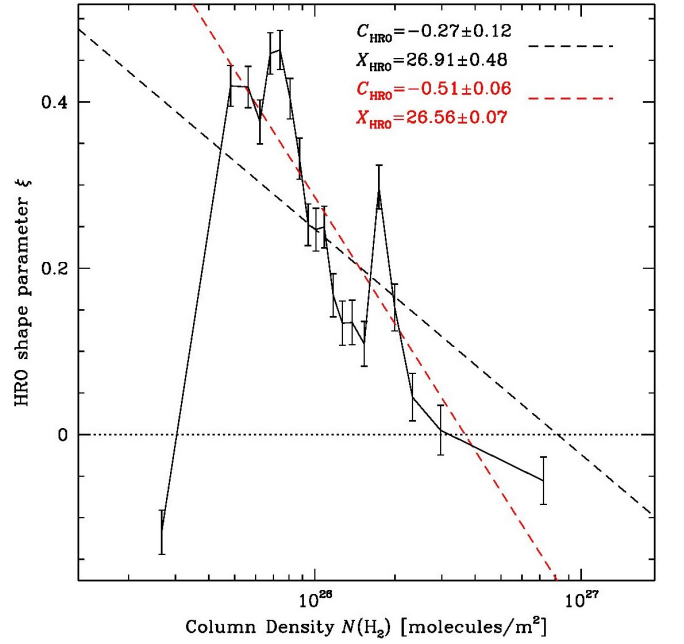


Figure 13. HRO shape parameter ξ as a function of column density N as fitted in Figure 12. The black labels and dashed line are solutions to the parameters C (the slope) and X (log of the N -axis intercept) of a linear regression to all the ξ data, while the red labels and dashed line are for a fit to all bins except the first ($\log N < 25.64$), which includes the lowest-S/N $\theta_{B\perp}$ data.

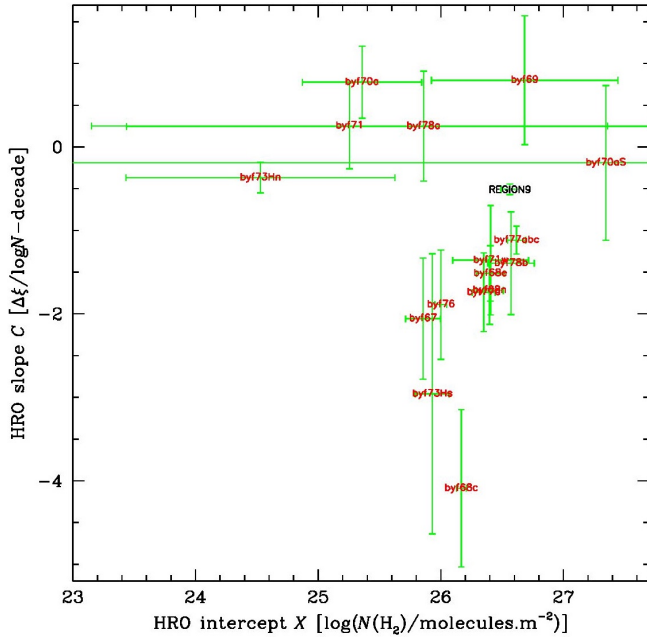


Figure 14. Results of HRO regression analysis in each ROI shown in Appendix C, except for BYF 70aN which lies far outside the plot window at $(X,C) = (25.75, 7.56)$. These are shown with the clump’s name in red at the fitted (X,C) coordinates, each with green error bars from the formal fit uncertainties. In addition, we show in black the overall Region 9 result from Fig. 13.

For comparison, the overall Region 9 HRO result is shown in Figure 14 in black. From this we can see that the nominal group is fairly representative of the whole Region, in that the $\log N$ intercepts are all reasonably close to the Figure 13 value, while the slopes are all clearly negative, although the individual ROIs do have slopes *more* negative than the Region-wide average (respectively, -1 to -4 compared to -0.5). To some extent, one can attribute this trend to a reduction in statistical uncertainty: i.e., as the number of points in a ROI goes up, the slopes become less negative and less uncertain. Nevertheless, the average slope within the nominal group is -2.0 . Evidently, the contribution of the statistics from the other 7 ROIs seems to push the Region-wide slope to its less negative value, but without erasing its clearly negative (8σ) signal.

Otherwise, there doesn’t appear to be an obvious physical reason for some clumps/ROIs to give a clearly negative slope C_{HRO} , and for others to be flat or positive. For example, we can easily estimate an average T_{dust} across each ROI from the SED fits of Pitts et al. (2019), and plot this vs. the C_{HRO} slope with a linear fit as shown in Figure 15. This hints at a trend, in the sense of steeper slopes C_{HRO} as T_{dust} falls, i.e., a sharper transition to criticality in colder gas. This would make physical sense, in that gas that is warmer is expected to be more disturbed from its cooler, more SF-prone state, where gravity is primarily only resisted by B fields. But the correlation shown here is not very strong, and would need better evidence to be considered reliable. However, we return to this idea in §4.

Instead, inspection of the individual ROI B_{\perp} -vector maps is a little more informative (Figs. 3–5). Since any anomalies may be most obvious in the outlier or flat ROIs, we consider them first.

BYF 70aN, outlier. In Pitts et al. (2019)’s SED-fit N_{H_2}

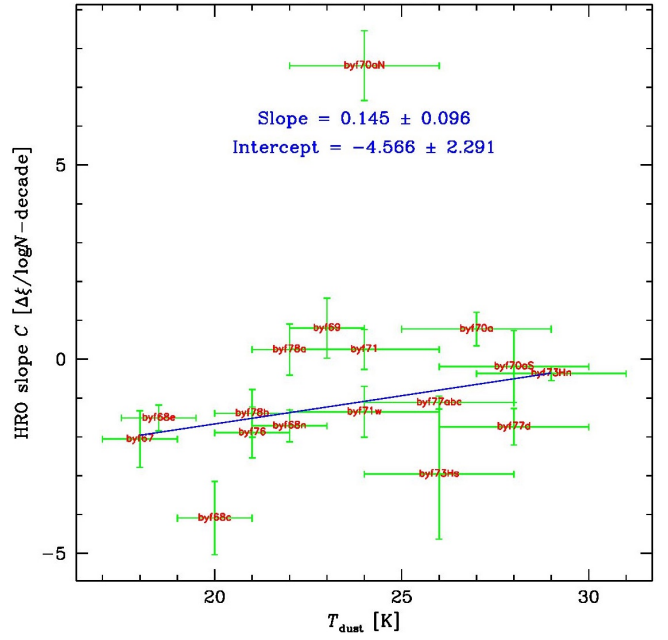


Figure 15. Comparison of HRO C_{HRO} slope parameter vs. mean T_{dust} across each of the 17 ROIs. Also shown is a linear fit in this space (blue) to the 16 ROIs excluding BYF 70aN, with correlation coefficient $r = 0.37$ and other parameters as labelled.

map, this ROI lies across an area of relatively flat $N \sim 0.5 \times 10^{26}$ molec/ m^2 , but which nevertheless peaks along a ridge which is well-aligned with most of the $\theta_{B_{\perp}}$ values, $+20^{\circ} \pm 10^{\circ}$. This accounts for the strongly positive ξ values at the highest- N bins in its matching HRO plot (App. C), while the alignment tends to perpendicularity going down the ridgeline ($\xi < 0$ at low- N). Because of the apparently “crushed” B field configuration (possibly due to the expanding edge of the NGC 3324 HII region), the nominal ξ trend is reversed.

BYF 69, flat. The $\theta_{B_{\perp}}$ distribution here is strongly peaked again at $-20^{\circ} \pm 20^{\circ}$, although projected to be about 3 pc away from it. The polarisation signal is also displaced from the peak N structure, so the angular correlation is poor, tending to perpendicularity everywhere and leading to a weakly positive ξ - N trend.

BYF 70a, flat. This ROI is centred on the sharpest N gradient at the edge of the HII region, and most B_{\perp} vectors are aligned with its strong ionisation front, so there is an overall dominance of parallel alignments and another weakly positive HRO.

BYF 70aS, flat. Just south of the previous ROI, the data here straddle what appears to be a breakout in the ionisation front, judging by the anticorrelation of the N map with $\theta_{B_{\perp}}$. That is, where N is high, we see a dominantly parallel/north-south B field alignment, such as would be produced by the HII region’s overpressure. Where there is a gap in N along the front, the field lines turn sharply east-west as if to trace an escape route for the HII. The ξ - N trend is therefore very flat.

The above four ROIs seem to be strongly affected by the radiation and dynamical overpressure from the NGC 3324 HII region. One surmises that the kind of delicate, pre-stellar interplay between B fields and gravity has been swamped here by post-SF feedback.

BYF 71, flat. Once again, the $\theta_{B_{\perp}}$ distribution is completely uniform at $-60^{\circ} \pm 20^{\circ}$, and again parallel to the

edge of the HII region despite being projected $\sim 1\text{--}4$ pc away from it. Its rising-then-falling HRO plot, however, seems to be strongly affected by the 2 lowest- N bins showing perpendicular alignments off the NW edge of the N map. Otherwise, this ROI may actually follow the nominal ξ - N pattern, including the high-density peaks inside the clump's NW edge.

BYF 73Hn, flat. Despite being part of BYF 73's compact HII region, and therefore sampling mostly post-SF gas, the HRO trend is vaguely nominal, although statistically weak (slope/error = 2).

BYF 78a, flat. This ROI has 3 distinct $\theta_{B\perp}$ correlation patches within it, the 2 smaller of which straddle a higher-density feature and align with its contours, at least in part, in the nominal way. The third patch has $\theta_{B\perp}$ perpendicular to the low- N contours going away from the higher-density feature, so generate a positive ξ - N trend there. The area seems to be somewhat dominated by its surroundings.

In the 10 nominal ROIs, their B fields do not obviously appear to be influenced by NGC 3324 or its ionisation front. Their negative ξ - N slopes suggest that those clump areas conform to the presumption of the HRO method, i.e., that the balance between B fields and gravity shifts from magnetic at low columns to gravitic at high columns. One might then argue that the functional reason for a clump exhibiting a nominal ξ - N plot vs. a flat or reversed ξ - N is whether the gas is dominated by slow internal forces (nominal) or more dynamic external forces. Brief remarks on the 10 ROIs follow.

BYF 67, nominal. This clump has a distinctly elliptical shape in N_{H_2} , peaking at 5×10^{26} molec/m², with a low-ish average $T_d = 18 \pm 1$ K. However, its polarisation signal is concentrated on its eastern side and has highest p' off the N peak. Thus, most of its B_{\perp} vectors are aligned approximately radially to the N distribution, although at the lowest N contours, the alignment becomes more oblique.

BYF 68, nominal. This clump's appearance in N is rather amorphous with somewhat cool $T_d = 20 \pm 2$ K, but its HAWC+ data self-partition into three ROIs. In the central ROI, BYF 68c contains a similar mixture of radial and circumferential p' vectors to BYF 67, with more of the latter at lower N and vice versa. The eastern BYF 68e, however, has a strongly aligned p' field across its elongated shape, in such a way as to produce a consistently nominal HRO diagram. Last, the northern BYF 68n has a distribution of p' vectors intermediate between c and e.

BYF 71w, nominal. West of the bulk of BYF 71, this ROI consists of a strongly polarised ridge with its p' vectors mostly aligned along it, similar to the elongated parts of BYF 71 but without the confusion at the low- N contours.

BYF 73Hs, nominal. Again part of BYF 73's compact HII region sampling post-SF gas, the ξ - N trend is still statistically weak (slope/error = 2) but more negative than in BYF 73Hn.

BYF 76, nominal. This clump is again somewhat amorphous in N but has a well-ordered p' field. The net result is a clearly negative ξ - N slope but with some variance.

BYF 77abc, nominal. These 3 clumps are nestled close to each other near the southern boundary of NGC 3324,

in a complex area of elevated $T_d = 25\text{--}30$ K and N_{H_2} up to $\sim 5 \times 10^{26}$ m⁻². They are compact (\sim beam-sized) at the Mopra resolution ($37''$; indeed, BYF 77b is itself a double) but BYF 77b & c resolve into a ~ 1.6 pc-wide shell at the higher HAWC+ resolution ($14''$), with BYF 77a projected to be 1 pc outside this shell to the southwest. They are considered together because the HAWC+ polarisation vectors are remarkably well-aligned ($\theta_{B\perp} = 55^\circ \pm 30^\circ$) across all these features, and in the same direction as the maximum extent of the complex, from a to c. As such, they give a strongly nominal ξ - N plot once the lowest- N bin (with poor S/N) is discounted.

BYF 77d, nominal. This 4th clump in the BYF 77 complex is far enough away (3 pc projected to the SW) to be clearly separated in both the Mopra and HAWC+ maps, but it is also distinguished by having a different $\theta_{B\perp}$ distribution ($20^\circ \pm 25^\circ$) than in a-c. This gives a distinctly nominal HRO plot, but conversely with a slightly rising ξ trend at the higher N bins.

BYF 78b, nominal. The negative ξ - N trend in this cooler ($T_d = 21 \pm 1$ K) clump is clear, but a little confused by a mixture of alignments at the higher N levels.

Besides these intercomparisons, we also briefly consider some similar HRO studies in other SF regions, as discussed by Barnes et al. (2023). These employed *Planck*, *Herschel*, BLASTpol, and HAWC+ data to investigate various Gould Belt, Vela-C, and L1688 clouds (Planck Collaboration 2016; Soler et al. 2017; Zucker et al. 2020; Lee et al. 2021). The other instruments had lower angular resolution than HAWC+, but since these clouds are all closer to us than Region 9/ η Car, most of these studies obtained a similar sub-parsec physical resolution as herein. However, the clouds studied have a typical column density from much- to somewhat-lower than the average in Region 9.

The typical threshold column densities X for this HRO work were about 0.6 (Gould), 3 (Vela-C), and 0.6 (L1688) $\times 10^{26}$ m⁻². Our all-Region 9 value from Figure 14 is $X = 3.6 \times 10^{26}$ m⁻². Thus, Region 9 seems to contain clumps that not only have higher column and volume densities in general than a number of local ($d < 1$ kpc) clouds and complexes, but also have criticality (i.e., the threshold for balancing gravity with magnetic pressure support) displaced to higher densities as well.

We can also compare the respective equivalent B_{crit} field strengths derived in the nearby clouds with the values obtained here. From Eq. (4) we can write

$$B_{\text{crit}} \text{ (nT)} = N_{\text{H}_2} / (1.57 \times 10^{25} \text{ m}^{-2}) \quad (6)$$

where $\lambda = 1$, i.e., where $N_{\text{H}_2} = X_{\text{HRO}}$. Then, $B_{\text{crit}} \sim 4$ nT for the Gould Belt (Planck Collaboration 2016), ~ 20 nT for Vela-C (Soler et al. 2017), and ~ 4 nT for L1688 (Lee et al. 2021). Similarly, for Region 9 as a whole, $B_{\text{crit}} = 23 \pm 4$ nT, while for the 10 ROIs with nominal HRO trends, B_{crit} ranges over 5–27 nT. This places Region 9 at a higher- N_{crit} and $-B_{\text{crit}}$ level compared to these other clouds, when mapped at sub-pc scales. The equivalent B_{crit} result for the BYF 73 ALMA data is $B_{\text{crit}} = 42 \pm 7$ nT (Barnes et al. 2023), which is commensurate with the higher density levels on the 0.1 pc scale.

4. DISCUSSION

The results of the DCF analysis can be summarised as: the mapped B_{\perp} and $\log \lambda$ values show a generally

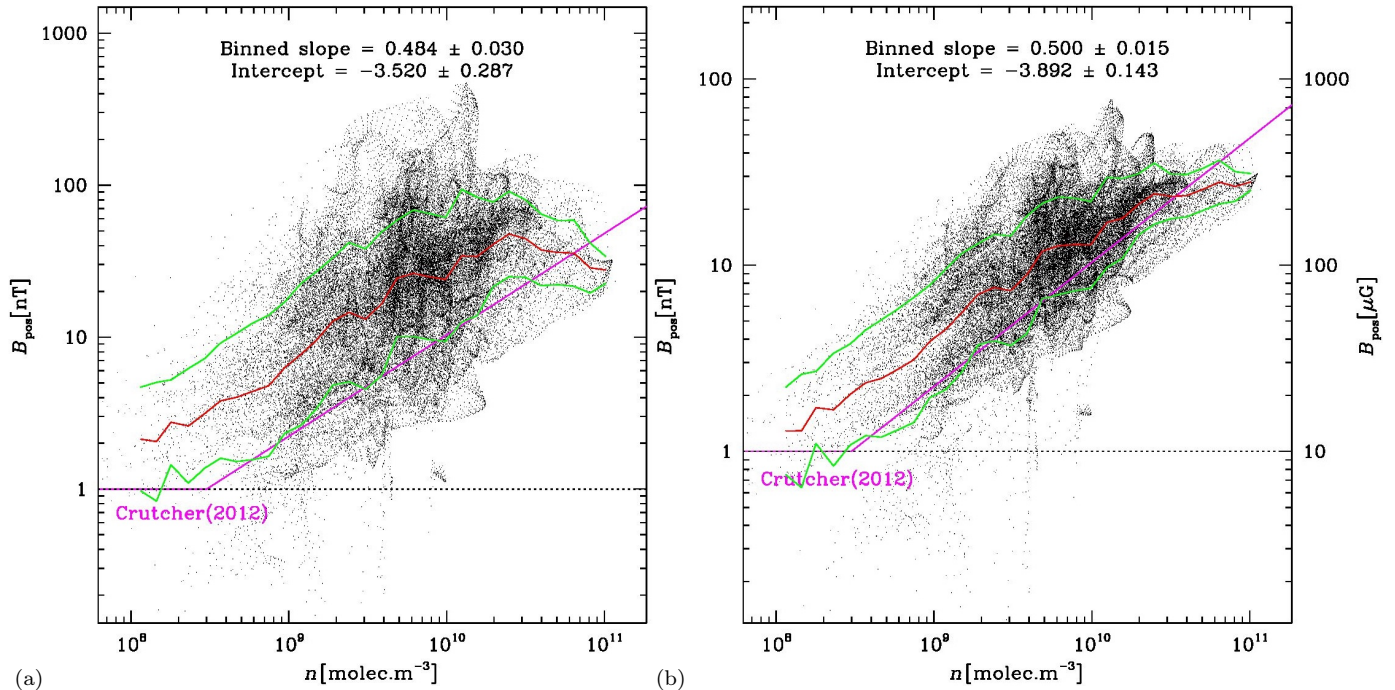


Figure 16. (a) Comparison of pixel values for B and n maps across all of Region 9 using the classical DCF calculation (Pattle et al. 2022), overlaid by the Crutcher (2012) relationship in magenta. The $\log B$ values were also averaged in each of 30 bins in $\log n$, and the bins’ mean ($\pm 1\sigma$) $\log B$ values are overlaid in red (green). The label at the top describes a linear fit to the binned means (i.e., a power-law fit to the linear data), with correlation coefficient $r = 0.95$ and $\chi^2 = 0.59$. A simple linear fit to all the $\log B$ - $\log n$ data at once gives a similar result, with slope $\kappa = 0.524 \pm 0.004$, intercept -3.80 ± 0.04 , and $r = 0.50$. Below a density threshold of $2.5 \times 10^{10} \text{m}^{-3}$, however, the binned means clearly trend close to the Crutcher (2012) slope of $\frac{2}{3}$, but displaced above it by a factor of ~ 2.5 , although the S/N in the B values tends to be low for $B < 10 \text{nT}$. (b) Similar to (a) but using the Skalidis & Tassis (2021) calculation for B . The distribution of points and fits are very similar, except for a smaller scatter in the ordinate due to the weaker dependence on s . Thus, the trend in low- n data is only a factor ~ 1.5 above the Crutcher (2012) line, and the high- n turnover is noticeably softer. A cgs scale is also shown on the far right.

slightly subcritical group of molecular clumps, at somewhat higher than typical column densities N . The results of the HRO analysis can be summarised as showing a clear trend towards criticality as N rises, but without clearly crossing into criticality over most of the mapped area. Encouragingly, we view these results as mutually compatible, and speak to the higher than typical B_{\perp} environment in these high-density clumps with only moderately vigorous SF. Exceptions to these statements do occur, but only in a few locations (most obviously, BYF 73).

The overall impression from the comparisons in §3.3 is that “environment matters.” In other words, since gravity is a weak force, and since the many B field studies summarised by B - n diagrams (e.g., Pattle et al. 2022) show that magnetic forces only seem to be of \sim similar strength to gravity in star-forming (i.e., dense) gas, any other effects that might buffet a cold, dense molecular cloud need to be at a fairly minimal level in order for the transition to criticality to occur. Specifically, strong feedback from a nearby classical HII region can potentially disrupt this process, even several pc beyond its own ionisation front. This is made visually intuitive in the LIC image of Appendix D.

More generally, the other HRO studies cited above show that the actual transition to criticality can happen at different column densities which seem to be location-dependent. Region 9 seems to be at the higher end of column densities N generally, and transition columns X in particular (e.g. 1 vs $3 \times 10^{26} \text{m}^{-2}$), than in most of the local clouds in the prior studies. At the same time,

when we zoom in to core scales (i.e., $< 0.1 \text{pc}$) like the MIR2+Streamer results from Barnes et al. (2023), we find both N generally and X specifically are higher still ($7 \times 10^{26} \text{m}^{-2}$).

This general trend holds also for the derived B_{\perp} values seen in Figs. 7a–10a. Overall, they range from ~ 10 – 200nT , with a few excursions higher, up to 470nT (or in old-fashioned cgs units, ~ 0.1 – 2mG , up to almost 5mG). As recently as a decade ago, mG fields had been rarely observed in star-forming clouds, according to the data of Crutcher (2012). More recent work has started to fill in this high- B space (up to $\mu\text{T}/10 \text{mG}$ fields) in massive star forming clouds, e.g., Cortes et al. (2024); the compilations of Pattle et al. (2022) and Whitworth et al. (2024) provide another ~ 20 measurements with $B > 100 \text{nT}$.

Yet here, in just a fraction of one GMC, we have 455 independent pixels with $B > 100 \text{nT}$, or 5% of our high-S/N data, mostly in and around some of the clump peaks (see Figs. 7a–10a).³ Perhaps the η Car clouds are unusual in their B field strengths, limiting SF to areas where the column density (and gravity) build up to a level sufficient to overwhelm such strong fields only where $\log \lambda$ is high, yielding massive SF in only select locations.

To illustrate this, we place our data in the B - n diagram (Fig. 16a). There, the line of criticality coincides approximately with the Crutcher (2012) relation-

³ This amplification of analytical capability, 9000 independent data points with polarisation S/N > 3 , compared to the more modest number of clumps targeted (17), was enabled by the gradient technique, Eq. (3), to estimate n at each pixel.

ship, with supercritical areas (gravity dominant) below that line and subcritical areas (B fields dominant) above it. Most of Region 9 is subcritical, trending towards criticality at only the highest densities ($\sim 10^{11} \text{m}^{-3}$), where the B fields are more modest ($\sim 30 \text{nT}$). By contrast, the strongest B fields (150–500 nT) occur at modest densities ($10^9\text{--}10^{10} \text{m}^{-3}$).

Using this diagram to obtain a slope κ in the Bn relationship for Region 9, we can support values of either $\sim \frac{1}{2}$ or $\sim \frac{2}{3}$ from our DCF-derived data, depending on the analysis method. Apparently due to sensitivity limitations, we also cannot find evidence for a density threshold n_0 where κ transitions to a lower value. But the strong turnover of the piecewise κ from $\frac{2}{3}$ over most of the observed range of n , to a value < 0 where $n > 2.5 \times 10^{10} \text{m}^{-3}$, suggests a possible breakdown at high density of the main assumption of DCF, that it arises from incompressible Alfvén waves, as discussed by Pattle et al. (2022).

Variants of this analysis give very similar results. For example, retaining a correlation length of 0.5 pc from the DCF procedure instead of the assumed 0.33 pc (Appx. A) raises slightly the overall dispersion s in the distribution of polarisation angles, correspondingly lowering the resulting B_{\perp} values to some extent. A single, whole-sample power-law fit then gives $\kappa = 0.499 \pm 0.003$, intercept = -3.72 ± 0.03 , and $r = 0.55$, virtually identical to the result in Figure 16a. Fitting the binned data, we obtain $\kappa = 0.462 \pm 0.025$, intercept = -3.44 ± 0.24 , $r = 0.96$, and $\chi^2 = 0.40$, again very close. However, for $\log n < 10.5$, the trend does soften somewhat, from $\kappa \approx \frac{2}{3}$ to 0.566 ± 0.013 , intercept = -4.37 ± 0.12 , $r = 0.99$, and $\chi^2 = 0.99$, mainly because the pixels most affected by the different choice of correlation scale tend to be the ones where s was small and B large to begin with. In this case, the maximum $B_{\perp} = 158 \text{nT}$ and we only wind up with 79 independent pixels above 100 nT, or about 1% of our data. But otherwise, the overall data distribution looks very similar to Figure 16a, including the displacement of the mean trend by a factor of ~ 2 above the Crutcher (2012) line, and the turnover to $\kappa < 0$ for $\log n > 10.5$.

However, when we recast the Bn diagram with Eq. (2) from Skalidis & Tassis (2021), we find a somewhat more noticeable effect on the data distribution (Fig. 16b). Since the scatter in the ordinate of the Bn diagram is mostly due to the scatter in s , Eq. (2)'s weaker dependence on s produces a more compressed distribution, including having no data points with $B > 100 \text{nT}$. Interestingly, the turnover to smaller κ at high n is much softer, suggesting that Skalidis & Tassis (2021)'s formalism may not have the same high- n issues as has been suggested for classical DCF. However, the plots in Figure 16 do not indicate a clear preference for classical DCF vs. the Skalidis & Tassis (2021) analysis.

Pattle et al. (2022) have also pointed out that the trends in the Bn diagram are somewhat built-in, since with DCF measurements, B and n are not independent (see Eq. (1)). Absent other factors, we would expect $\kappa = \frac{1}{2}$, and so any structure in this diagram is really measuring the Alfvén number, M_A . In the classical DCF analysis, this reduces to

$$M_A = s/Q, \quad (7)$$

where s is now in radians and $Q \approx 0.5$ usually: we show

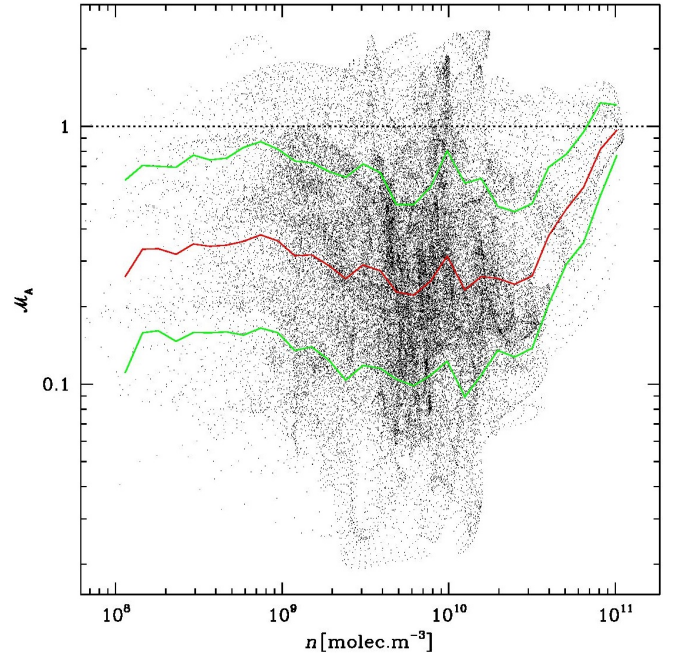


Figure 17. Alfvén number as a function of density in Region 9. The bin means $\pm 1\sigma$ are shown merely to indicate trends.

this for the Region 9 data in Figure 17. We recover much the same pattern as do Pattle et al. (2022), where most clouds are sub- or trans-Alfvénic. There, M_A is typically $\sim 0.2\text{--}2$ and flat with n , but at $n \gtrsim 10^{12} \text{m}^{-3}$, M_A rises significantly to 10 or more, suggesting a change to criticality. In Region 9, this turn-up seems to begin at $10^{10.5} \text{m}^{-3}$, but only rises to $M_A \approx 1$.

We can also examine criticality more directly through $\log \lambda$. From §3.1, the overall $\log \lambda$ distribution across Region 9 is rather close to gaussian at a mean of -0.75 (this is when we use the classical DCF B_{\perp} values). That is, the average λ is 0.35, meaning somewhat strong support against gravity in most areas. Only a rather small fraction of pixels (2%) have this reversed, $\lambda > 3$.

But if environment matters, then perhaps the gas or dust temperature is as important as the column density, as far as the transition to criticality is concerned. We therefore reconsider the T_{dust} evidence first raised in §3.3, but in a more structure-independent way, i.e., pixel by pixel as shown in Figure 18a. The much larger $|r|$ than in Figure 15 suggests a significant trend despite the large scatter in $\log \lambda$ within each bin. An (unbinned) simple linear fit gives similar slope and intercept but $r = -0.14$, suggesting a weaker overall correlation. However, what matters to SF is where the gas has positive $\log \lambda$.

For example, if we count the fraction of pixels within each T_{dust} bin with $\log \lambda > 0$ (i.e., $\lambda > 1$) as representative of gas more likely to be gravitationally dominated, then accumulate these statistics into T_{dust} quintiles in order to reduce the bin-to-bin fluctuations, the fractions are 12.4% for $T_{\text{dust}} = 17.6\text{--}20.5 \text{K}$ (1st quintile), 7.0% for $20.5\text{--}23.4 \text{K}$ (2nd quintile), 2.3% for $23.4\text{--}26.7 \text{K}$ (3rd quintile), 3.7% for $26.7\text{--}29.6 \text{K}$ (4th quintile), and 0.08% for $29.6\text{--}32 \text{K}$ (5th quintile). This seems to demonstrate a real trend towards significantly more high- λ gas as T_{dust} falls.

This impression is more formally supported with a t -

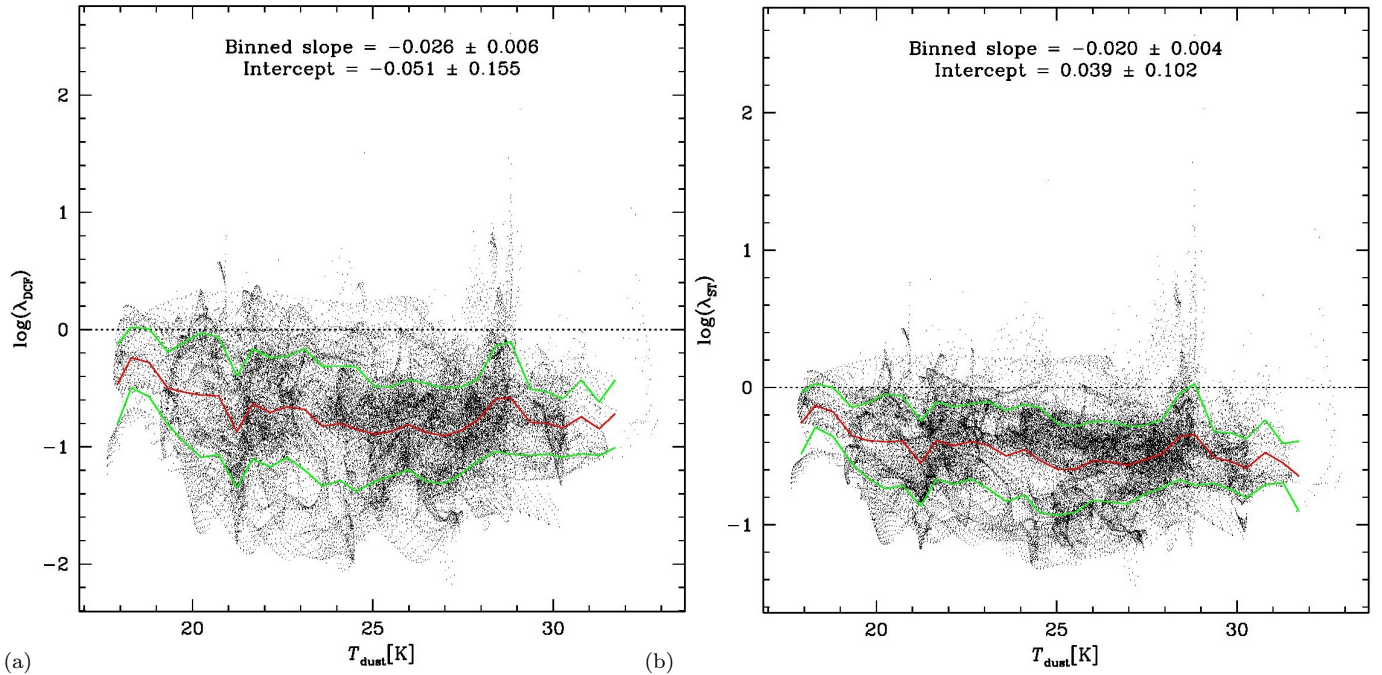


Figure 18. (a) Comparison of pixel values for $\log\lambda$ and T_{dust} maps across all of Region 9 using the DCF formula for B_{\perp} , Eq. (1). The λ values were also averaged in each of 30 bins in T_{dust} , and the bins’ mean ($\pm 1\sigma$) $\log\lambda$ values are overlaid in red (green). The label at the top describes a linear fit to the binned means, with correlation coefficient $r = -0.63$ and $\chi^2 = 0.55$. (b) Same as (a) but using the Skalidis & Tassis (2021) formula for B_{\perp} , Eq. (2). Here the fit to the binned means has $r = -0.68$ and $\chi^2 = 0.24$.

statistic, of the form

$$t = \frac{\bar{x} - \mu}{(\sigma/\sqrt{n})}, \quad (8)$$

where \bar{x} is the mean of a (small) test sample, μ is the mean of a parent population, σ is the dispersion in the population, and n is the test sample size. We take the 23 highest- T_{dust} bins (i.e., $21 \text{ K} < T_{\text{dust}} < 32 \text{ K}$) to define the hypothetical “normal” sample of molecular clouds, based on the appearance of the mean trend (red) in Figure 18a. This population has a mean $\log\lambda = -0.78 \pm 0.44$ (1σ). We then compute the t statistic for the 7 lowest- T_{dust} bins (i.e., $17.7 \text{ K} < T_{\text{dust}} < 20.9 \text{ K}$), both individually and collectively, and these are listed in column 4 of Table 1. In column 5 of each case is listed the probability of the null hypothesis (that the bin is drawn from the same population as the “main sample”) being satisfied.

We compare again how the Skalidis & Tassis (2021) analysis changes these results (Fig. 18b). Superficially, the $\log\lambda$ distribution (still very close to gaussian) is systematically shifted to higher values compared to classical DCF, the mean increasing by 0.3 in the log ($2\times$ higher in λ). But the distribution around this mean is also compressed, with the dispersion dropping from 0.44 to 0.31 in the log (25% smaller in λ). The end result is that the overall statistical trends are very similar to the classical DCF approach. The fraction of points with $\log\lambda > 0$ in the same T_{dust} quintiles are now 8.8%, 6.7%, 3.2%, 5.0%, and 0.8% respectively, and the t -statistics are listed in columns 6 & 7 of Table 1. While the quintile trend is now more muted, the t -statistics still strongly reject the null hypothesis.

Thus, with either approach, each low- T_{dust} bin shows a highly significant difference between its $\log\lambda$ distribution and that of the warmer bins. In other words, colder

Table 1

Region 9 $\log\lambda$ t -statistics and probabilities for low- T_{dust} bins using DCF formulae, Eqs. (1) and (2)

Bin	Sample Size ^a	Mean T_{dust} [K]	DCF		ST	
			t	Prob.	t	Prob.
1	368	17.9	5.49	$<10^{-4}$	5.83	$<10^{-4}$
2	455	18.3	10.54	$<10^{-4}$	10.02	$<10^{-4}$
3	325	18.8	8.21	$<10^{-4}$	7.40	$<10^{-4}$
4	929	19.3	7.86	$<10^{-4}$	5.69	$<10^{-4}$
5	1255	19.8	8.07	$<10^{-4}$	4.90	$<10^{-4}$
6	1695	20.3	8.42	$<10^{-4}$	5.22	$<10^{-4}$
7	1795	20.7	8.43	$<10^{-4}$	5.75	$<10^{-4}$
1–7	6822	19.8	20.7	$<10^{-4}$	15.30	$<10^{-4}$
8–30	45518	25.5	0	—	0	—

^a The sample size refers to the number of pixels in the pipeline-rendered SOFIA data. These images oversample the HAWC+ beam by a factor of 2.5 compared to Nyquist. Therefore, we have divided the sample sizes by 2.5² for the number of degrees of freedom (i.e., independent measurements) in the probability calculation.

clouds are statistically more likely to be dominated by gravity, and not supported by magnetic fields. Such a result comports well with the relationship between T_{dust} and N_{H_2} in massive clumps (Pitts et al. 2019; Pitts & Barnes 2021). They found a strong trend of falling T_{dust} as N_{H_2} rises towards the centres of around 85–90% of all CHaMP clumps on the sub-pc scale, as determined by SED fitting to far-IR/submm data. This trend fails to appear in only about 10–15% of clumps, accompanied by either strong internal heating from massive SF at clump centres or strong external heating from nearby massive SF, changing such clumps’ original pre- or protostellar internal state. Taken together, the SED fits and results here suggest that we can add a trend of rising λ to the internal prestellar state of massive clumps, as a systematic feature of massive SF.

5. CONCLUSIONS

Based on new SOFIA/HAWC+ far-IR continuum polarisation data, we have presented a systematic study of the 0.16–30 pc scale magnetic field in 17 of 21 massive molecular clumps comprising the western end of the η Carinae GMC (Region 9 of CHaMP, $d = 2.5$ kpc). The polarisation data were analysed in order to learn about the structure, strength, role, and significance of the B field in this cloud. Our results include the following.

- The HAWC+ polarisation data are widely distributed but do not cover all the known far-IR emission features of these clumps at the sensitivity levels we had originally planned to reach.

- DCF analysis of the polarisation directions (i.e., B_{\perp} magnetic field orientations) shows correlation lengths (areas within which the field is well-aligned) of ~ 0.5 – 1.5 pc in the various clumps. We adopted a scale 0.33 pc for subsequent calculations, in order to avoid numerical instabilities in mapping the orientation dispersion. We also mapped the representative gas density across the clumps, estimated as the gradient of the column density. Combining these with a published velocity dispersion map, we mapped B_{\perp} and the mass-to-flux ratio λ across the HAWC+ data, using both classical and modern DCF formulae.

- HRO analysis of all the HAWC+ data show a strong transition to criticality at $\log(N_{\text{crit}}/(\text{molec m}^{-2})) = 26.56 \pm 0.07$, reflecting the nominal HRO pattern of B field alignments with gas structures. For individual clumps, only 10/17 display the same nominal HRO pattern, with $(\mu \pm \sigma) \log N_{\text{crit}} = 26.27 \pm 0.25$. The other 7 clumps show atypical HRO patterns with B fields affected by external forces, most notably the radiation or overpressure from the nearby HII region NGC 3324.

- Region 9 has both stronger B fields and higher column density N relative to similar studies of more local clouds. The distribution of data in the Bn diagram is mostly parallel to but slightly above the Crutcher (2012) relation, then dropping below it at $n \gtrsim 10^{10.5} \text{ m}^{-3}$. The $\log \lambda$ distribution is close to gaussian, with $\mu \pm \sigma = -0.75 \pm 0.45$ (classical DCF) or -0.49 ± 0.31 (Skalidis & Tassis 2021), i.e., most areas are subcritical (B dominant). With either approach, there is a small but significant excess of areas above this distribution with $\log \lambda > 0$ (super-critical), but the Region as a whole appears to have sufficient magnetic support to explain the low star formation efficiency.

- In addition to the existence of critical transition densities from magnetic to gravitational domination, lower dust temperatures also seem to trace a significantly higher likelihood of criticality in such gas. This is consistent with previous studies of T_{dust} dropping towards high- N peaks at the centres of massive clumps (Pitts et al. 2019; Pitts & Barnes 2021).

Despite molecular clouds’ wide observational diversity, the physical keys to star formation in massive clumps may boil down to a balance between external heating, internal radiative cooling, and gravity’s slow but inexorable force overcoming the support of magnetic fields, as clouds’ central densities rise and gas temperatures drop.

We lament the grounding of SOFIA, and thank the aircraft crew and instruments’ scientific staff for their

outstanding support of this pioneering facility. We also thank Prof. Enrique Vázquez-Semadeni for suggesting the Skalidis & Tassis (2021) analysis, and the anonymous referee for helpful comments which improved the presentation of several points in the paper. PJB gratefully acknowledges financial support for this work provided by NASA through awards SOF 07-0089 and 09-0048 issued by USRA. This paper is based in part on observations made with the NASA/DLR Stratospheric Observatory for Infrared Astronomy (SOFIA). SOFIA was jointly operated by the Universities Space Research Association, Inc. (USRA), under NASA contract NNA17BF53C, and the Deutsches SOFIA Institut (DSI) under DLR contract 50 OK 2002 to the University of Stuttgart.

Facilities: SOFIA(HAWC+).

Software: Jupyter, karma, Miriad, SuperMongo.

REFERENCES

- Barnes, P. J., Yonekura, Y., Fukui, Y. et al. 2011, ApJS, 196, 12
 Barnes, P. J., Li, D., Telesco, C., et al. 2015, MNRAS, 453, 2622
 Barnes, P. J., Hernandez, A. K., O’Dougherty, S. D., Schap, W. J. III, & Muller, E. 2016, ApJ, 831, 67
 Barnes, P. J., Hernandez, A. K., Muller, E., & Pitts, R. L. 2018, ApJ, 866, 19
 Barnes, P. J., Ryder, S. D., Novak, G., Crutcher, R. M., Fissel, L. M., Pitts, R. L., & Schap, W. J. III 2023, ApJ, 945, 34
 Cabral, B. & Leedom, L. C., 1993, “Imaging Vector Fields Using Line Integral Convolution,” Proc. 20th ann. conf. *Computer graphics and interactive techniques* (SIGGRAPH ’93: Anaheim, CA), pp. 263–270
 Chandrasekhar, S., & Fermi, E. 1953, ApJ, 118, 113
 Cortes, P. C., Girart, J. M., Sanhueza, P., et al 2024, ApJ submitted, arXiv:2406.14663
 Crutcher, R. M., Nutter, D. J., Ward-Thompson, D. & Kirk, J. M. 2004, ApJ, 600, 279
 Crutcher, R. M. 2012, ARA&A, 50, 29
 Davis, L. 1951, Phys.Rev., 81, 890
 Fissel, L. M., Ade, P. A. R., Angilè, F. E., et al. 2016, ApJ, 824, 134
 Fissel, L. M., Ade, P. A. R., Angilè, F. E., et al. 2019, ApJ, 878, 110
 Gooch, R. E. 1997, Proc. Astr. Soc. Aust., 14, 106
 Harper, D. A., Runyan, M. C., Dowell, C. D., et al. 2018, *J. Astr. Instrum.*, 7(4), 184008
 Lazarian, A. 2007, JQSRT, 106, 225
 Lazarian A., Yuen K. H., Ho, K. W., et al. 2018, ApJ, 865, 46
 Lee, D., Berthoud, M., Chen, C-Y., et al. 2021, ApJ, 918, 39
 Liu, J., Zhang, Q., Qiu, K., 2022, Front. Ast. Space Sci., 9, 943556
 Lupton, R. & Monger, P. 2000, SuperMongo Manual, unpublished
 McKee, C. & Ostriker, E. 2007, ARA&A, 45, 565
 Myers, P. C., & Goodman, A. A. 1991, ApJ, 373, 509
 Ostriker, E. C., Stone, J. M., & Gammie, C. F., 2001, ApJ, 546, 980
 Pattle, K., Fissel, L., Tahani, M., Liu, T., & Ntormousi, E. 2022, to be published in *Protostars and Planets VII*, S.-I. Inutsuka et al., eds. (arXiv:2203.11179)
 Pitts, R. L., Barnes, P. J., Ryder, S. D., & Li, D. 2018, ApJ, 867, L7
 Pitts, R. L., Barnes, P. J., & Varosi, F. 2019, MNRAS, 484, 305
 Pitts, R. L., & Barnes, P. J. 2021, ApJS, 256, 3
 Planck Collaboration XXXV 2016, A&A, 586, A138
 Samson, W. B. 2021, J.Br.Astron.Assoc., 131(2), 97
 Sault, R. J., Teuben, P. J., & Wright, M. C. H., 1995. in “Astronomical Data Analysis Software and Systems IV,” eds. R. Shaw, H. E. Payne, J. J. E. Hayes, ASP Conference Series, 77, 433
 Skalidis, R. & Tassis, K., 2021, A&A, 647, A186
 Soler, J., Ade, P., Angilè, F., et al. 2017, A&A, 603, A64
 Whitworth, D. J., Srinivasan, S., Pudritz, R. E., et al. 2024, MNRAS, submitted (arXiv:2407.18293)
 Zucker, C., Speagle, J. S., Schlafly, E. F., Green, G. M., Finkbeiner, D. P., Goodman, A., & Alves, J. 2021, A&A, 633, 51

APPENDIX

A. DETAILS OF DCF ANGULAR DISPERSION ANALYSIS

Here we describe in detail the steps in the DCF analysis procedure for each of the clumps in the South, North, and West portions of Region 9 as desired in §3.1. We closely follow the procedure of Barnes et al. (2023), which requires defining an appropriate correlation length over which s is measured, as explained by Myers & Goodman (1991).

The correlation length can be intuitively understood by inspection of Figures 3–5. The polarisation vectors are seen to be closely correlated in direction over small patches of each HAWC+ field, typically of size 3–10 beamwidths (~ 0.5 – 1.5 pc). Beyond that scale, the vectors are less correlated, presumably signifying the scale within which the B field is also physically correlated (i.e., sampling the MHD wave in one domain). We need to quantify this behaviour more precisely, and especially, to map it.

We first fit the distributions of the rotated polarisation position angle θ_B across a given map area with a simple gaussian $e^{-\theta_B^2/2s^2}$ to obtain a best-fit value for the dispersion s in θ_B (measured in radians) over that area. The problem then reduces to deciding what areas are appropriate to collect these statistics. To bracket the scales described above, we collect s data from a HAWC+ beam scale to complete patches above the S/N limit for each clump (or part-clumps with distinct θ_B patterns).

In the HAWC+ data, the measured $\theta_{B\perp}$ in any given region with S/N $\gtrsim 5$ will have an uncertainty in orientation dominated by instrumental noise, $\Delta\theta_{B\perp} \lesssim 3^\circ$. This occurs at a level around $P' = 0.3$ Jy/beam in Figures 3–5, but even down to a formal S/N ~ 2 – 3 around such areas ($P' \sim 0.2$ Jy/beam), the polarisation signal will be correlated over small areas (a few beams) while the noise will not. Therefore, such data also contains useful information, and we show the corresponding $\theta_{B\perp}$ vectors in Figures 3–5 down to this lower level.

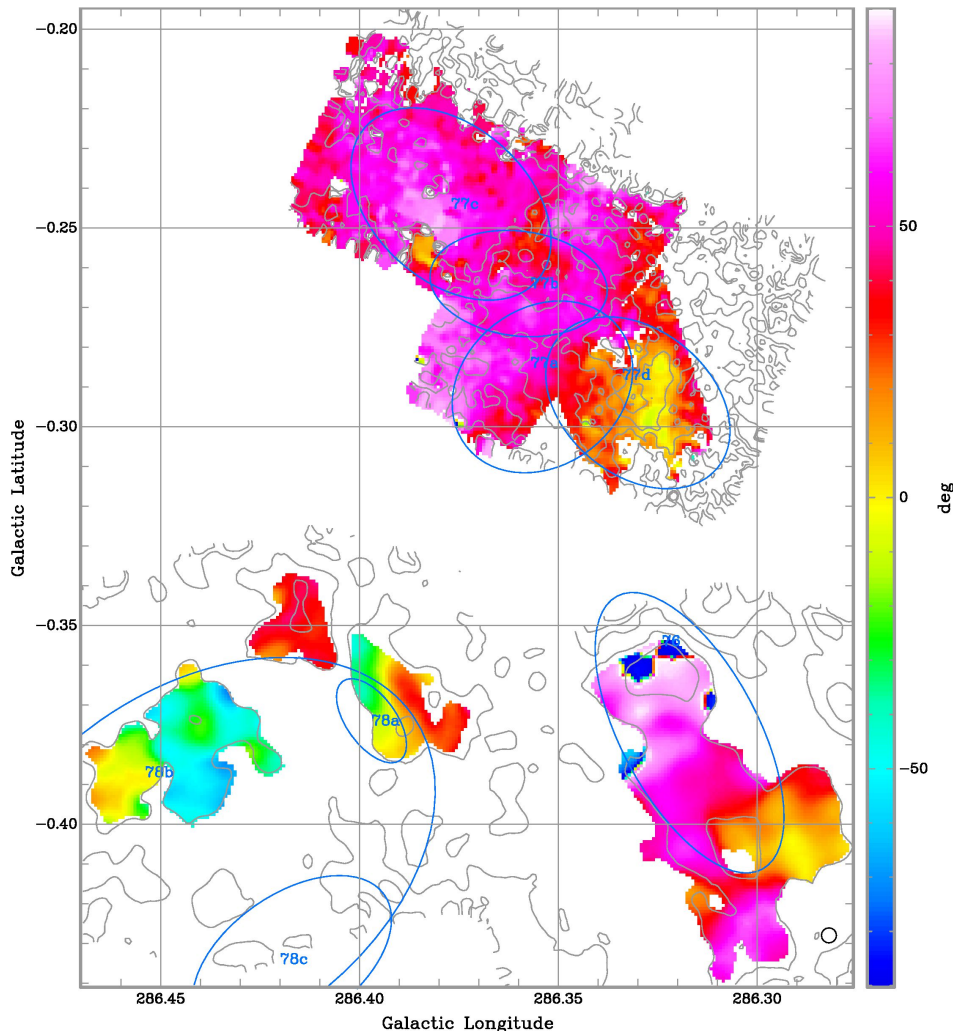


Figure A1. Cutouts of the $\theta_{B\perp}$ distribution in the Region 9 South ROIs (BYF 76, 77a–d, 78a–b) with S/N(P') $\gtrsim 5$, overlaid by grey P' contours at 0.2(0.4)1.0 Jy/bm and blue Mopra ^{12}CO ellipses. The DCF analysis for these ROIs appears in Fig. A2. For clump BYF 78c, the data were of insufficient S/N to be included in the DCF analysis.

In many of the Cycle 9 fields, this meaningful polarisation signal is detected over a number of irregular patches, but most are smaller than the individual fields. In the Cycle 7 fields, the brighter emission generally results in wider P' detections across each field. In either case, we can define regions of interest (hereafter ROI) where the θ_{B_\perp} pattern appears reasonably well-correlated, as a first cut for areas over which we want to evaluate s . Practically, the ROIs are usually clump- or sub-clump sized areas with contiguous θ_{B_\perp} data. This is illustrated for Region 9 South in [Figure A1](#) (details of the same treatment for Region 9 North & West follow). These ROIs typically have $S/N > 5$ over most of their interiors, with some edges having $S/N \sim 2-3$.

Having defined the ROIs, we can see in [Figure A2, left panel](#) the θ_{B_\perp} distribution in all pixels within each. While some of these are only approximately gaussian, we show these fits in order to illustrate effective dispersions in θ_{B_\perp} for the full ROIs. The point is that the distributions are relatively limited, meaning we have roughly enclosed the maximum correlation scale within each ROI.

We next construct histograms for subsets (comprised of square boxes of area A) of each ROI, computing a dispersion $s(A)$ in θ_{B_\perp} for each subset. The smaller the boxes, the more choice we have of where to fit them inside each ROI. We then compute a mean dispersion $\langle s_{\theta_{B_\perp}}(A) \rangle$ (\pm a standard deviation) in the field orientation for all small boxes of a given area A , no matter where they are placed within the ROI. Finally, in [Figure A2, right panel](#) we plot all such results as a function of box size $A^{1/2}$, ranging from a minimal useful size of $A = 3 \times 3$ pixels (roughly one Nyquist sample given the HAWC+ band D beam) to the full size of each ROI.

In each ROI, the mean dispersion $\langle s \rangle$ within all boxes of area A rises as the box size increases, meaning that θ_{B_\perp} is more correlated on small scales (e.g., $s \lesssim 5^\circ$ within ~ 0.3 pc), and becomes less correlated over longer distances ($s \gtrsim 10^\circ$ beyond ~ 1.5 pc). The scale at which s first starts to plateau is where we identify the correlation length as per Myers & Goodman (1991). Thus, the HAWC+ polarisation data suggest that, as far as the B field is concerned, the correlation length across all of Region 9 is $\sim 0.5-1$ pc.

In what follows though, we use a correlation scale length of 0.33 pc for computing s as a practical matter. This is because we wish to make a rough map of s for purposes of computing B_\perp , but the actual variations in θ_{B_\perp} are such that, on scales $\gtrsim 0.5$ pc we start to overlap more and more areas where the θ_{B_\perp} wrap across $\pm 90^\circ$ distorts the averaging, in a way that is difficult to compensate for. In other words, we choose to slightly underestimate s on these smaller scales, rather than grossly overestimating it on larger scales.

Thus, we can map the rms dispersion s in θ_{B_\perp} at each pixel, even if it is systematically a slight underestimate. But with a single correlation length, we are not limited by ROIs and can compute s at every pixel in the HAWC+ maps where the polarisation $S/N > 3$. This is shown in [Appendix B \(Fig. B1\)](#).

In the North, [Figure A3](#) shows the ROI cutouts with sufficient S/N in the P' signal to perform the analysis, while the two panels of [Figure A4](#) show the statistics of the θ_{B_\perp} distributions. [Figures A5](#) and [A6](#) reflect the same information for the West cutouts.

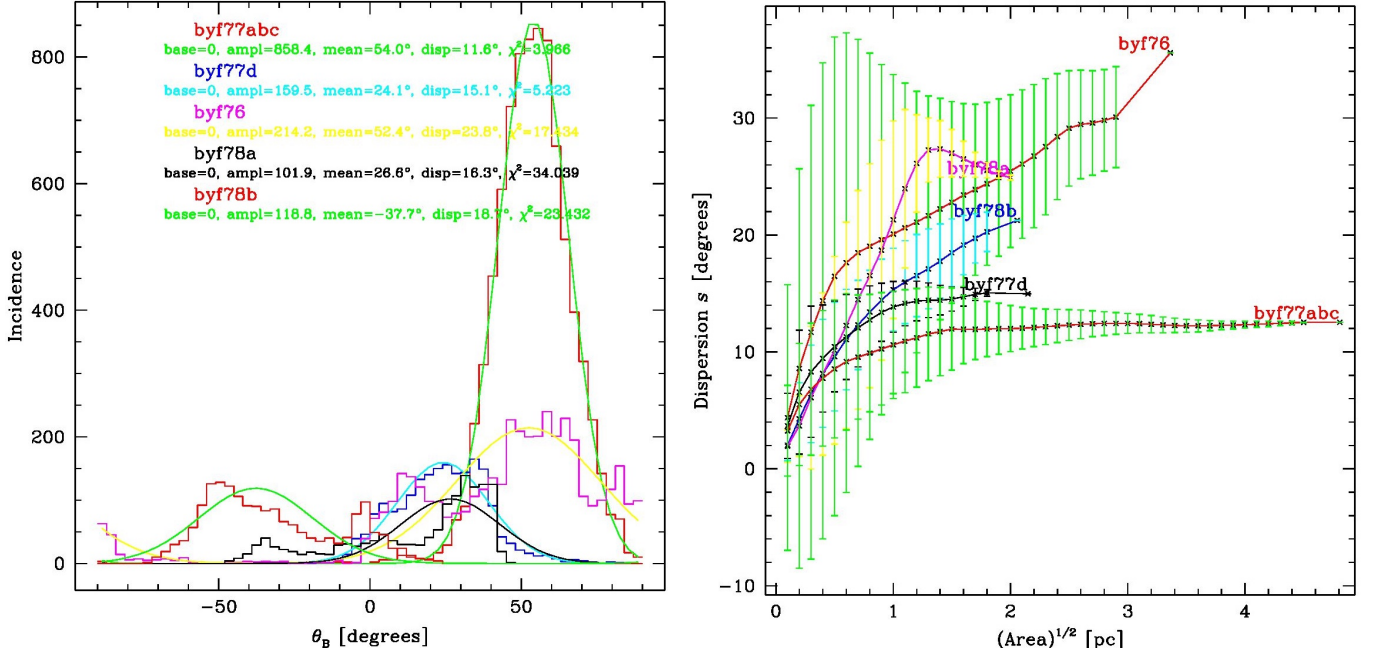


Figure A2. *Left:* Histograms of θ_{B_\perp} at all pixels within each of the ROI cutouts from Fig. A1, as labelled. Also shown are gaussian fits to each θ_{B_\perp} distribution, along with each fit's parameters. *Right:* Mean dispersion s of polarization position angles θ_{B_\perp} , with the 1σ variation in s shown as error bars, as a function of box size within each ROI shown in Fig. A1.

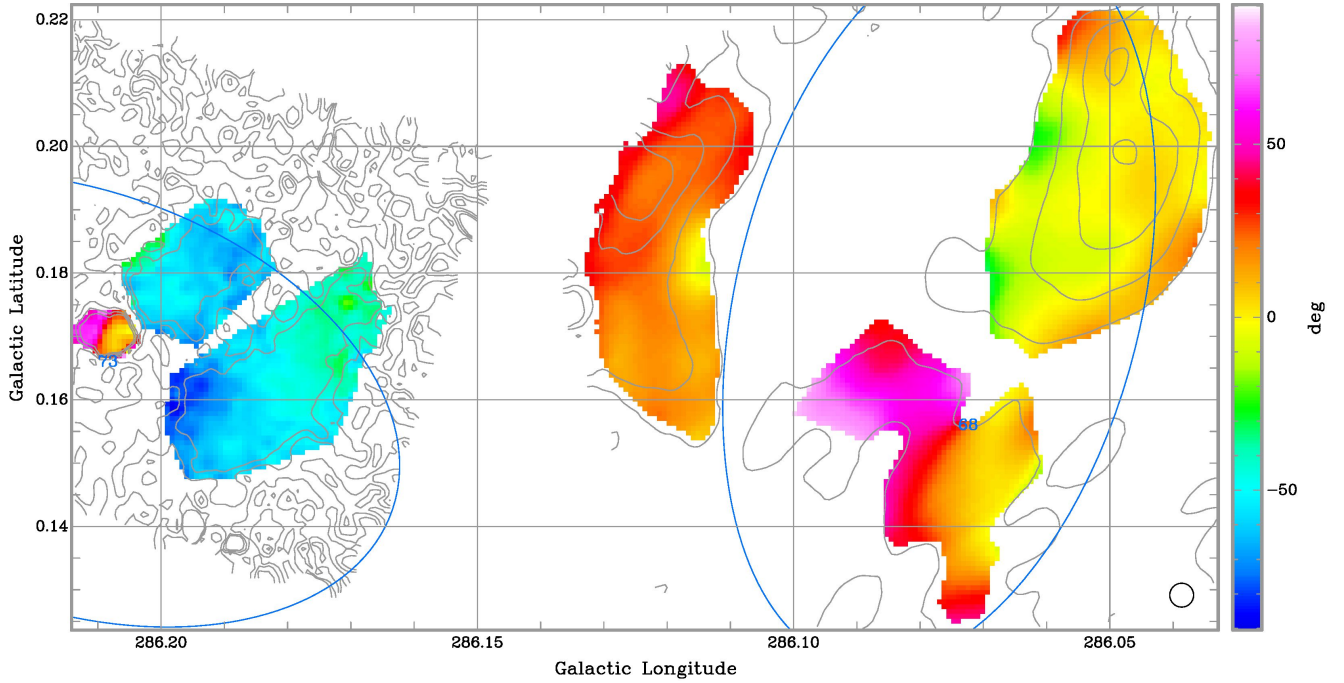


Figure A3. Cutouts of the $\theta_{B\perp}$ distribution in the Region 9 North ROIs (three for BYF 68 — centre, north, and east — and four for BYF 73 — north and south portions of the HII region, and the MIR2 and EPL portions of the massive core) with $S/N(P') \gtrsim 5$, overlaid by grey P' contours at 0.2(0.4)1.4 Jy/bm and blue Mopra ^{12}CO ellipses. The DCF analysis for these ROIs appears in Fig. A4.

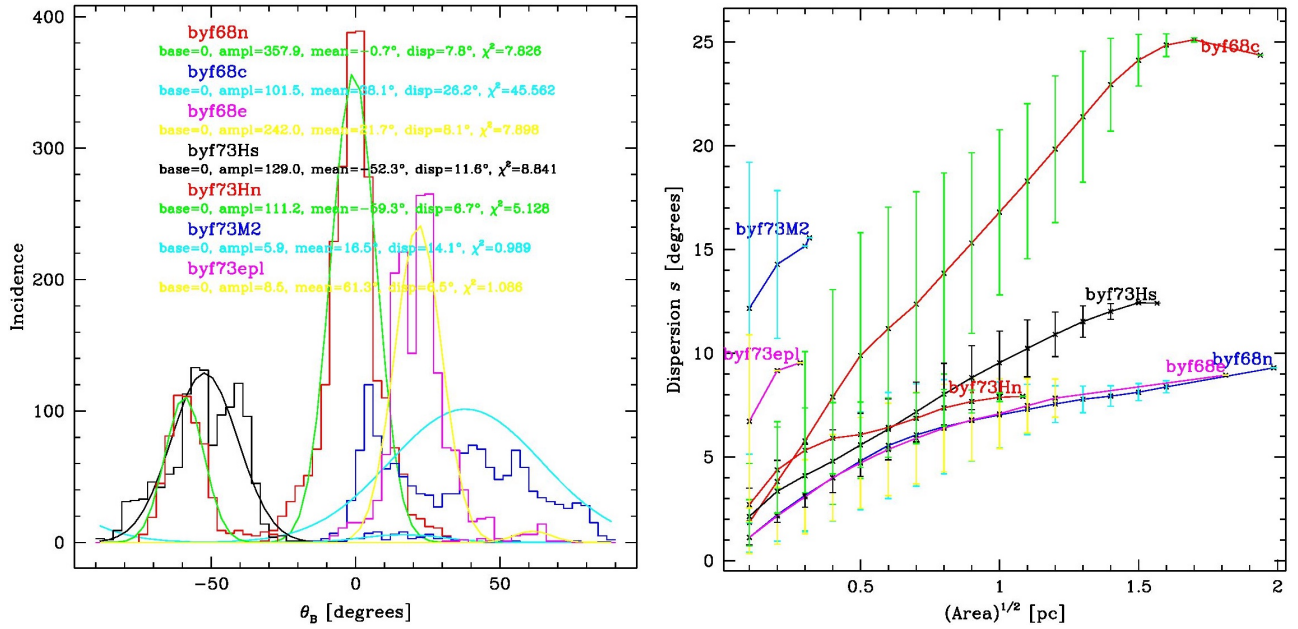


Figure A4. *Left:* Histograms of $\theta_{B\perp}$ at all pixels within each of the ROI cutouts from Fig. A3, as labelled. Also shown are gaussian fits to each $\theta_{B\perp}$ distribution, along with each fit's parameters. *Right:* Mean dispersion s of polarization position angles $\theta_{B\perp}$, with the dispersion in the dispersion shown as error bars, as a function of box size within each ROI shown in Fig. A3.

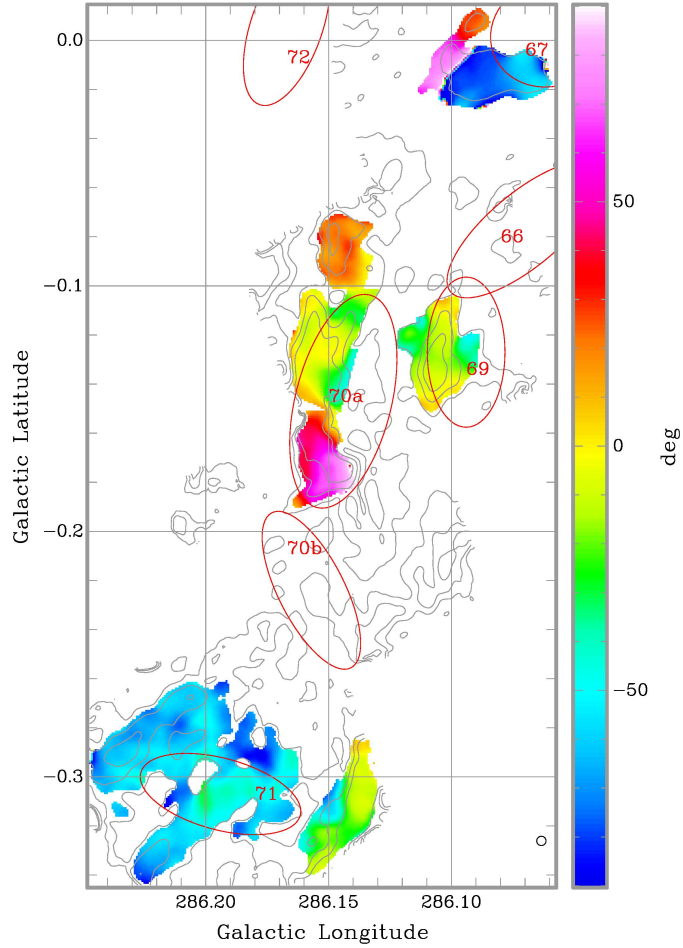


Figure A5. Cutouts of the $\theta_{B\perp}$ distribution in the Region 9 West ROIs (BYF 67, 69, three for BYF 70a — centre, north, and south — and two for BYF 71 — main and west) with $S/N(P') \gtrsim 5$, overlaid by grey P' contours at 0.2(0.4)1.0 Jy/bm and red Mopra ^{12}CO ellipses. The DCF analysis for these ROIs appears in Fig. A6. For clumps BYF 66 and 70b, the data were of insufficient S/N to be included in the DCF analysis.

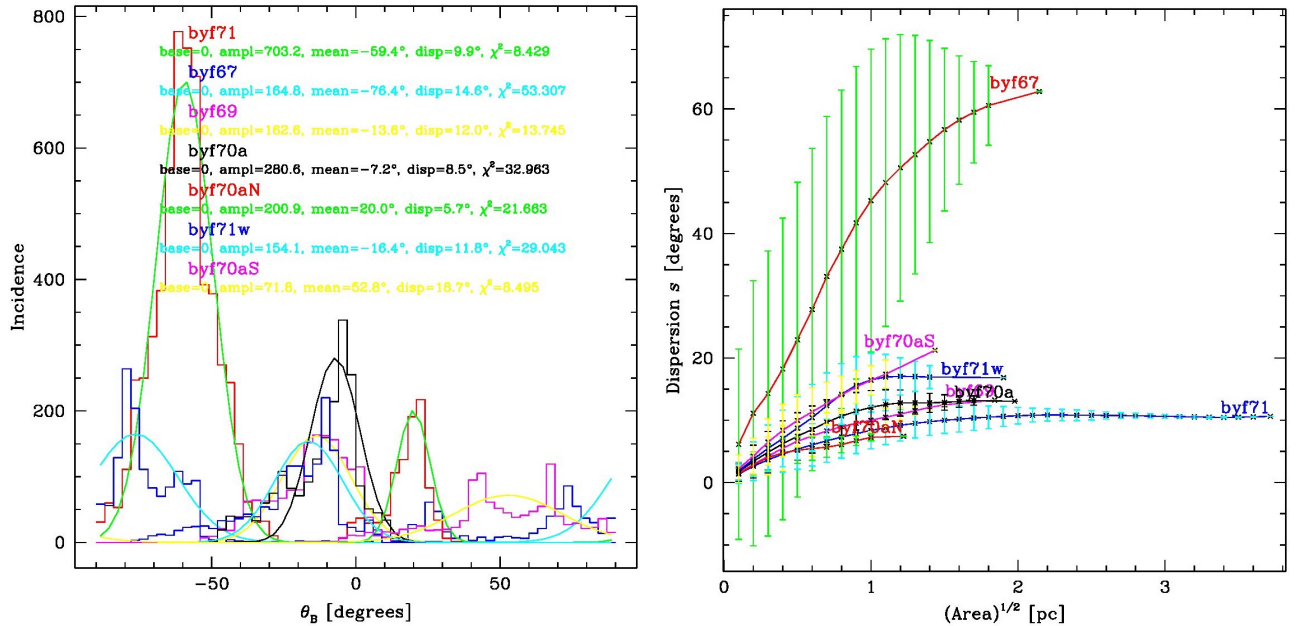


Figure A6. *Left:* Histograms of $\theta_{B\perp}$ at all pixels within each of the ROI cutouts from Fig. A5, as labelled. Also shown are gaussian fits to each $\theta_{B\perp}$ distribution, along with each fit's parameters. *Right:* Mean dispersion s of polarization position angles $\theta_{B\perp}$, with the dispersion in the dispersion shown as error bars, as a function of box size within each ROI shown in Fig. A5.

B. GLOBAL PARAMETER INPUTS TO B_{\perp} CALCULATION

Here we show the derived parameter maps for s , R , n , and ΔV , which are combined in Eq. (1) to produce the B_{\perp} maps shown in Figures 7–10.

We calculate s as follows. Starting with the HAWC+ $\theta_{B_{\perp}}$ maps, we make maps of (1) the local average of $\theta_{B_{\perp}}$ within the chosen correlation scale (0.33 pc), (2) the difference between each pixel's $\theta_{B_{\perp}}$ and this local mean, (3) the square of these differences, (4) the local mean of these squared differences on the same correlation scale as (1), and (5) the square root of this local mean. This is shown in Figure B1.

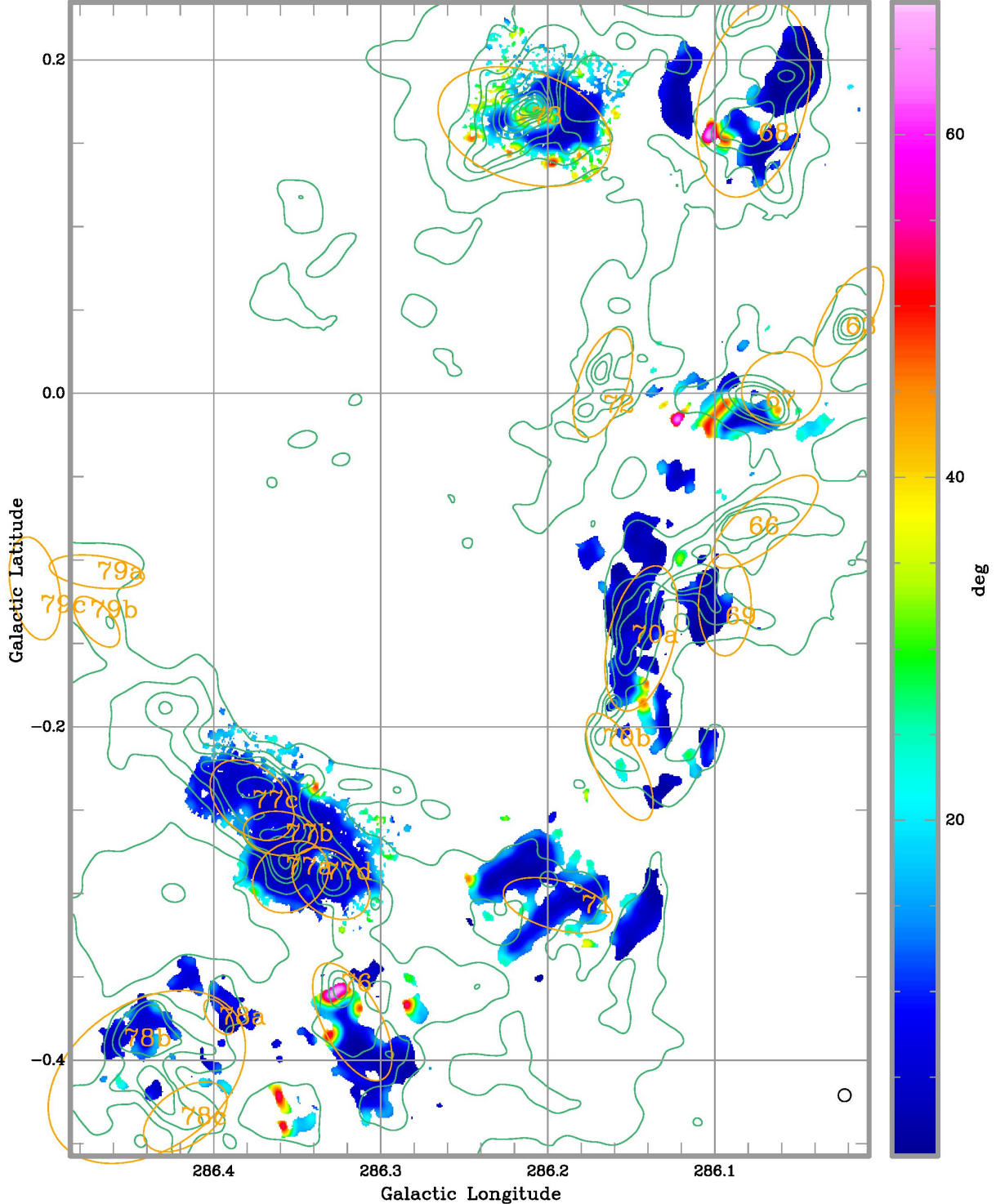


Figure B1. Complete Region 9 map of computed angular dispersion s from DCF analysis described in the text. Also overlaid, in this and subsequent figures, are green N_{H_2} contours at levels $0.5(0.5)2$ and $4(2)14 \times 10^{26}$ molecules m^{-2} and orange Mopra ^{12}CO half-power ellipses. The convolved beam size of the DCF analysis (twice the HAWC+ beam) is shown in the bottom-right corner.

Note that in most areas the s values are consistently small, $\lesssim 10^\circ$, on scales of $\sim 1\text{--}5$ pc across most of Region 9, and are more strictly $< 20^\circ$ over $\sim 95\%$ of the pixels; the modal range of values is flat-topped over $\sim 2\text{--}6^\circ$. The values become noticeably larger, however, only in small patches where the $\pm 90^\circ$ polarisation wrap occurs within the correlation scale, numerically distorting the s calculation. The only exception(s) where s is truly large ($\sim 30^\circ$) on these small scales is in the MIR 2 core of BYF 73, and in a few lower-S/N spots in BYF 67, 68, and 76.

We also show the derived R scale map as described in the main text (Fig. B2), mainly to demonstrate that the gradient method gives reasonable results for the HAWC+ data analysis. Most R values are well under 1.5 pc, although

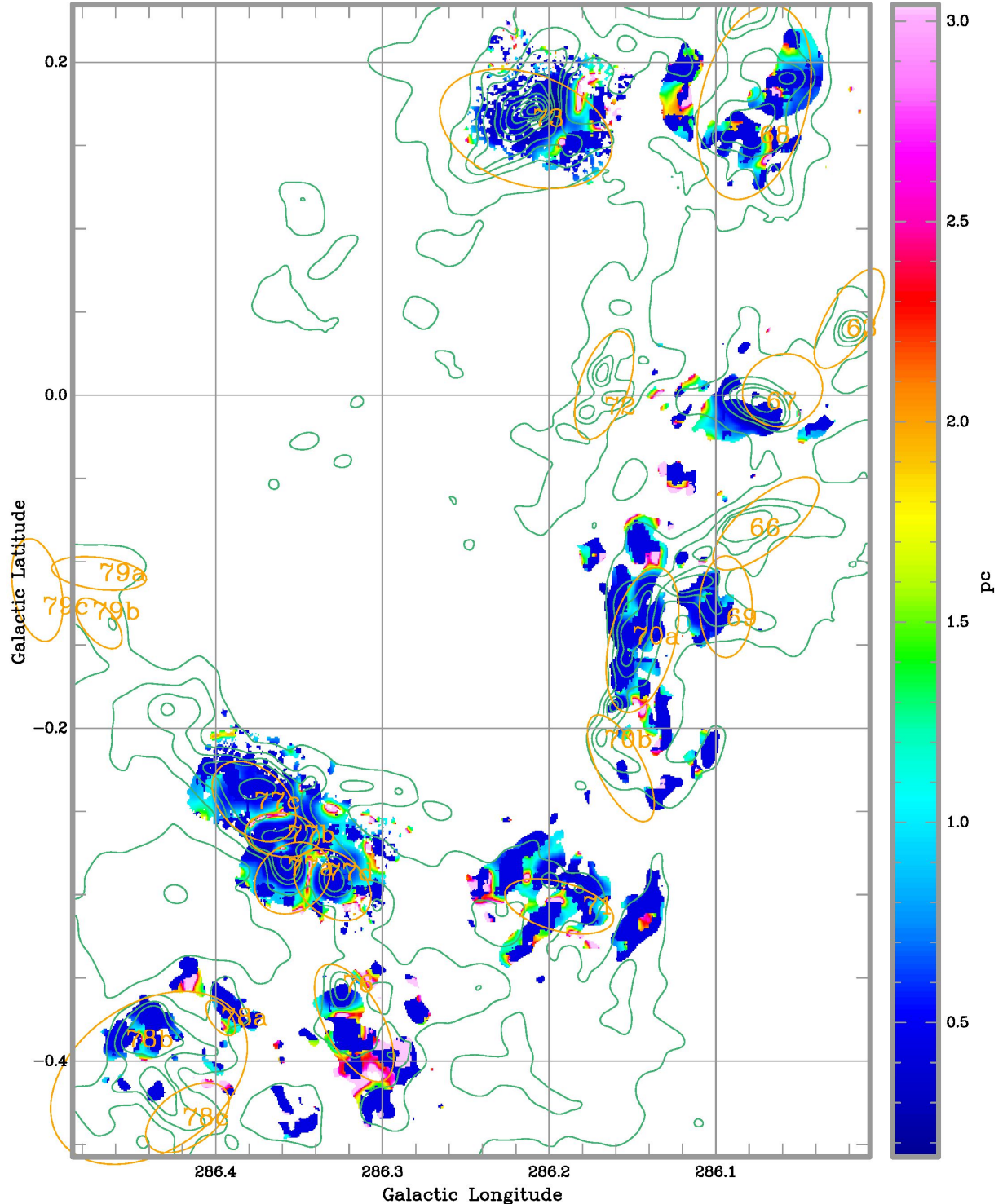


Figure B2. Complete Region 9 map of clump size/depth scale R as inferred from gradient method described in the text. The R values are computed on every pixel with available N data (e.g., Fig. B3), but masked to the s map in Fig. B1 to avoid visual clutter away from the polarisation signal.

small patches have $R > 5$ pc.

The n map (Fig. B3) obtained with our gradient method also appears satisfactory as a rough, structure-agnostic way to compute B_{\perp} .

Finally we show in Fig. B4 a σ_V map for the $N_{12\text{CO}}$ cube from Barnes et al. (2018), derived from a radiative transfer treatment of ^{12}CO , ^{13}CO , and C^{18}O data cubes that fully samples the opacity and column density in each line.

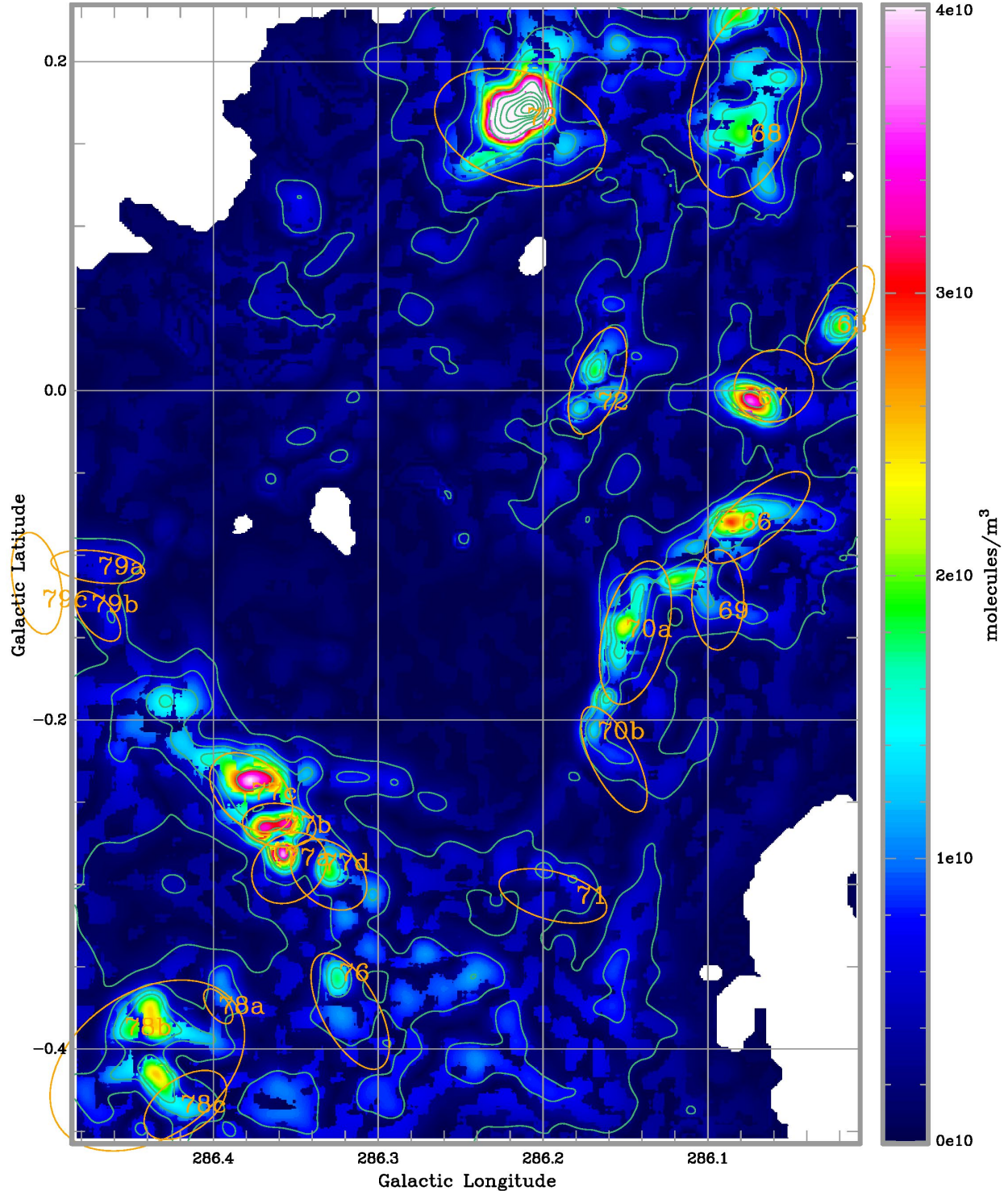


Figure B3. Complete Region 9 map of gas-phase molecular density n_{H_2} , derived from column density N_{H_2} map (Pitts et al. 2019) and gradient method to estimate R (Fig. B2) as described in the text. The colour scale displays most areas well, except for BYF 73 which is heavily saturated at a peak $n = 1.23 \times 10^{11} \text{ molecules m}^{-3}$.

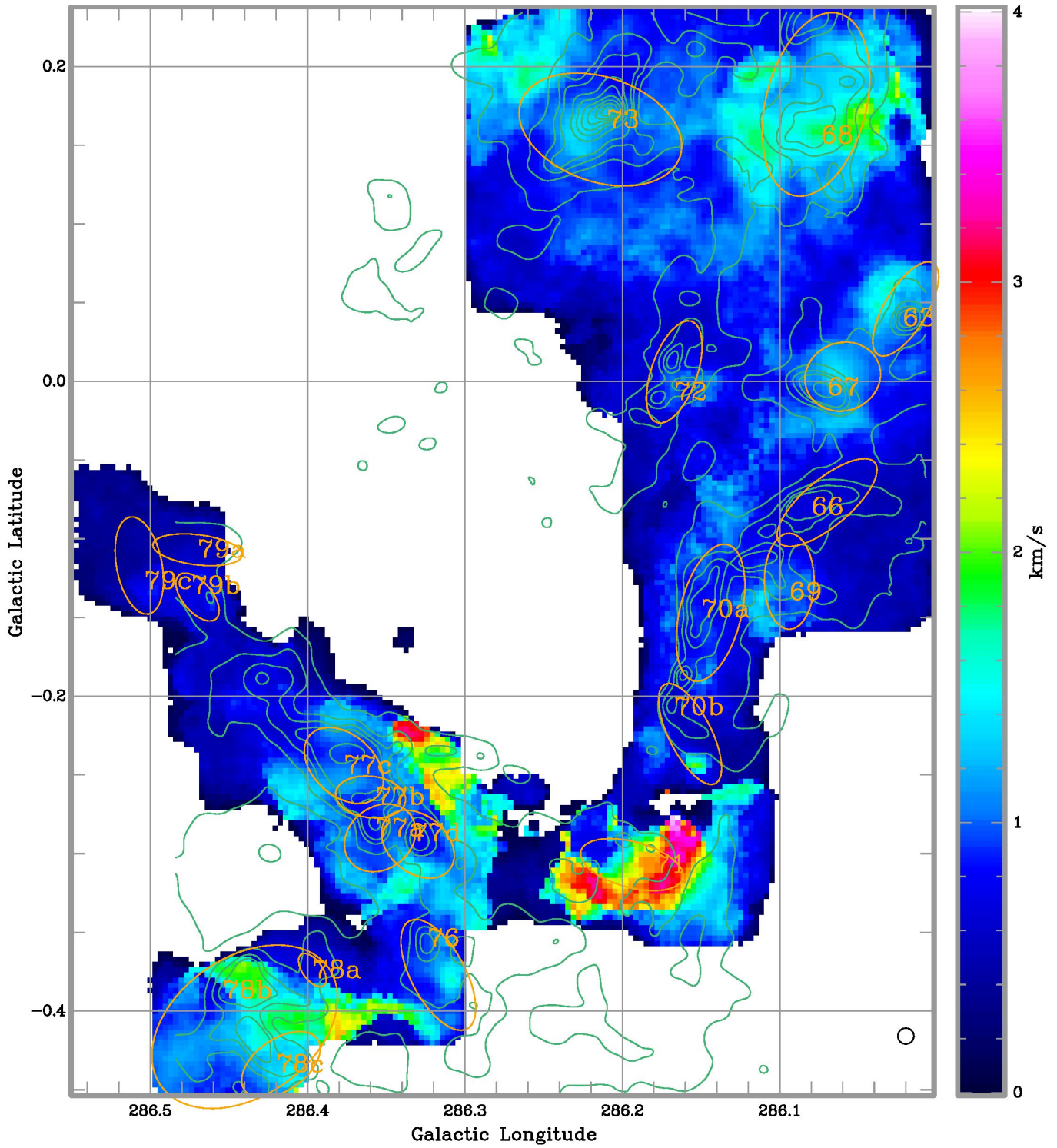


Figure B4. Complete Region 9 map of velocity dispersion from $N_{12\text{CO}}$ data (Barnes et al. 2018). The Mopra beam ($37''$) is shown in the bottom right corner.

C. HRO ANALYSIS OF INDIVIDUAL CUTOUTS

Figures C1 and C2 show 17 panels of the HRO analysis for individual ROI cutouts, out of 19 total ROIs. Each panel shows the relative orientation between the B field and gas structures (via the shape parameter ξ) as a function of column density N in each ROI, as in Fig. 13. In each ROI/panel we use only 10 bins in $\log N$ for the analysis, since the number of points available is (obviously) much smaller than for Region 9 as a whole (Fig. 13). Excluded are the plots for the 2 ROIs at the centre of BYF 73 (the MIR 2 core and EPL feature), since those ROIs are too small to be analysed by HAWC+ data alone. They were fully analysed with HAWC+ALMA data by Barnes et al. (2023).

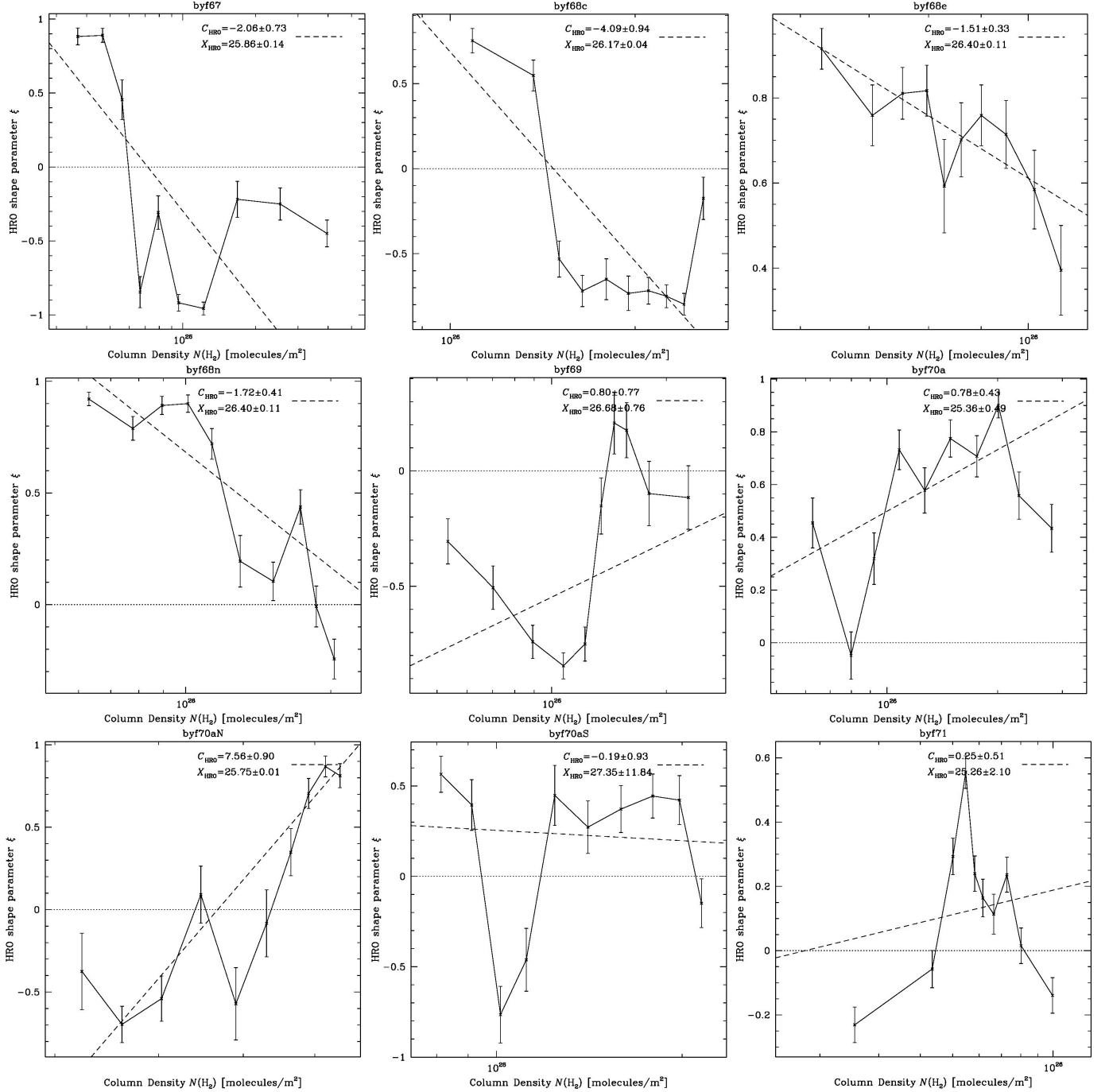


Figure C1. HRO analysis for 9 of the individual ROI cutouts shown in Figs. A1, A3, and A5, as labelled. The other panels are shown in Fig. C2.

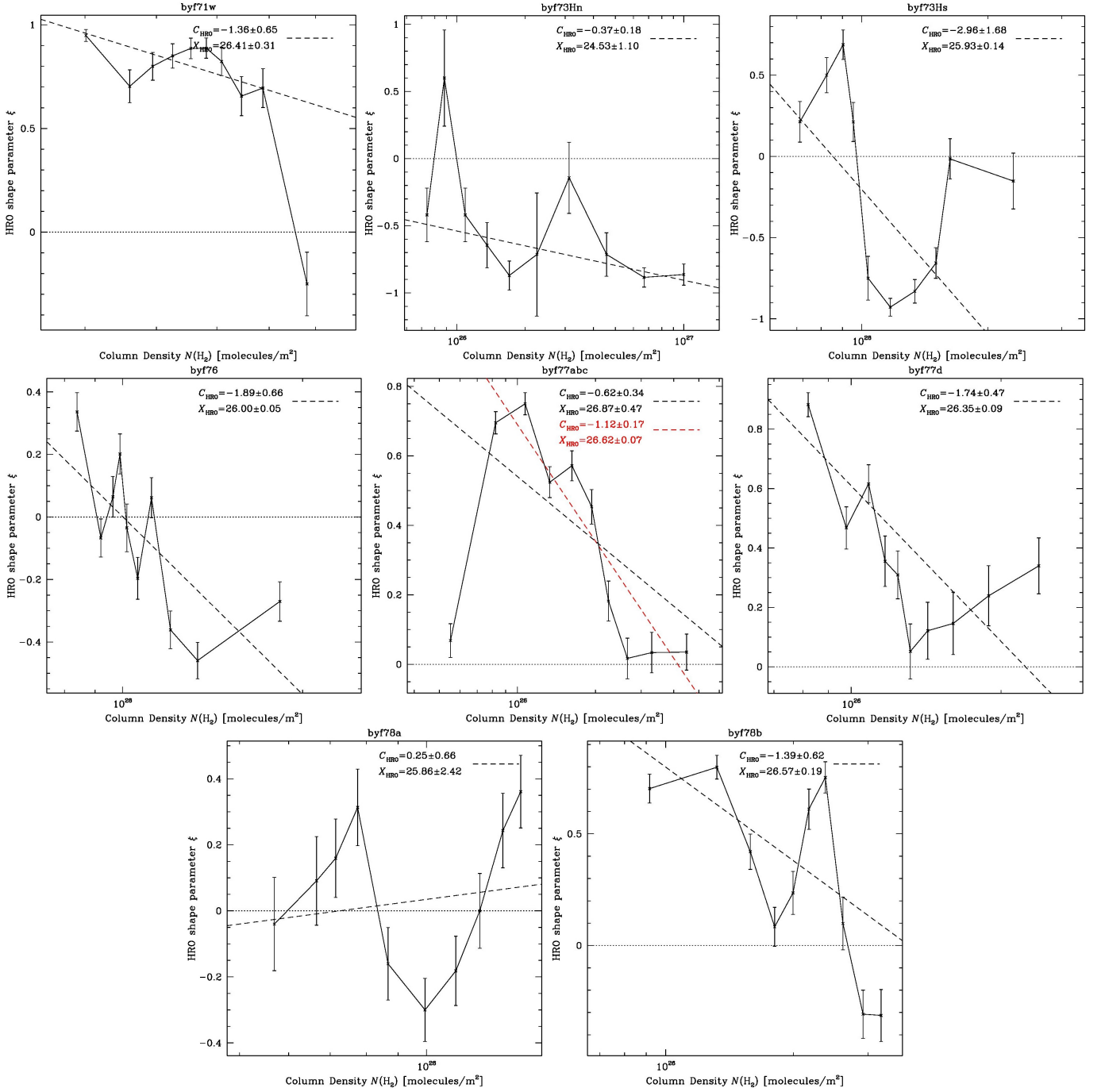


Figure C2. (Continuation of Fig. C1.) HRO analysis for 8 of the other 10 individual ROI cutouts shown in Figs. A1, A3, and A5, as labelled. In the panel for BYF 77abc only, we show two fits in red and black, where the red fit omits the first bin at low N and should be considered the more reliable fit, as in Fig. 13 and for the same reasons. None of the other panels required the same treatment.

D. LINE INTEGRAL CONVOLUTION IMAGE

We computed a LIC image (Cabral & Leedom 1993) of the *Herschel* data shown in Figure 1 based on the HAWC+ polarisation vectors of Figures 3–5; see **Figure D1**. This is useful as a visual confirmation of the preferentially circumferential B_{\perp} orientation around the NGC 3324 HII region and more bluish (= warmer) molecular clouds there, whereas the more reddish (= colder) molecular clouds that are further from the HII region’s influence seem to be unaffected by the HII region, magnetically speaking. This also contextualises the $T_{\text{dust}}\text{-log}\lambda$ trend seen in Figure 18.

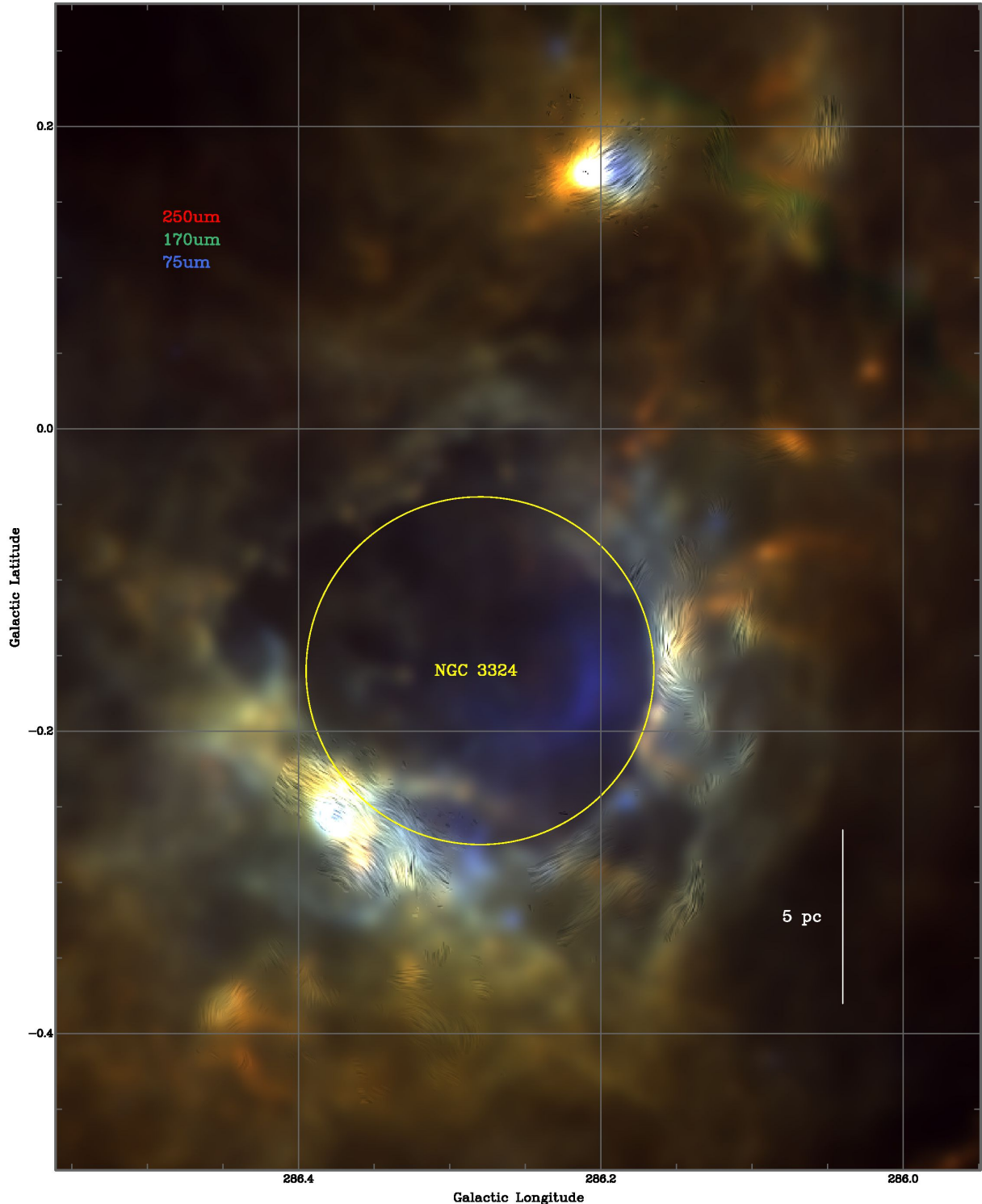


Figure D1. Line Integral Convolution (LIC) image of Region 9, obtained as follows. We started with a uniform noise map of the same size as the image shown; performed a one-dimensional 10-pixel convolution (the Line Integral) along the polarisation direction at each pixel in the noise map; multiplied the result by the polarisation amplitude at each pixel, normalised around unit brightness; and finally multiplied each colour channel in this image by the LICed noise map.